Mutation of the Mg^{2+} Transporter *SLC41A1* Results in a Nephronophthisis-Like Phenotype

Toby W. Hurd,* Edgar A. Otto,† Eikan Mishima,‡ Heon Yung Gee,† Hana Inoue,§ Masato Inazu,‖ Hideomi Yamada,¶ Jan Halbritter,† George Seki,¶ Masato Konishi,§ Weibin Zhou,† Tsutomo Yamane,** Satoshi Murakami,†† Gianluca Caridi,‡‡ Gianmarco Ghiggeri,‡‡ Takaaki Abe, ‡§§‖‖ and Friedhelm Hildebrandt†§§§‖‖‖

*MRC Human Genetics Unit, Institute of Genetics and Molecular Medicine, University of Edinburgh, Edinburgh, United Kingdom; †Department of Pediatrics, §§§Department of Human Genetics, and ‖‖‖Howard Hughes Medical Institute, University of Michigan, Ann Arbor, Michigan; ‡Department of Clinical Biology, Tohoku University Graduate School of Medicine, Miyagi, Japan; §Department of Physiology and ‖Institute of Medical Science, Tokyo Medical University, Tokyo, Japan; ¶Department of Internal Medicine, Faculty of Medicine, University of Tokyo, Tokyo, Japan; **Graduate School of Nanobioscience, Yokohama City University, Yokohama, Japan; ††Graduate School of Bioscience & Biotechnology, Tokyo Institute of Technology, Yokohama, Japan; ‡‡Istituto G. Gaslini, Genova, Italy; §§Division of Medical Science, Tohoku University Graduate School of Biomedical Engineering, Miyagi, Japan; and ‖‖Department of Clinical Biology and Hormonal Regulation, Tohoku University Graduate School of Medicine, Miyagi, Japan.

ABSTRACT

Nephronophthisis (NPHP)-related ciliopathies are recessive, single-gene disorders that collectively make up the most common genetic cause of CKD in the first three decades of life. Mutations in 1 of the 15 known *NPHP* genes explain less than half of all cases with this phenotype, however, and the recently identified genetic causes are exceedingly rare. As a result, a strategy to identify single-gene causes of NPHP-related ciliopathies in single affected families is needed. Although whole-exome resequencing facilitates the identification of disease genes, the large number of detected genetic variants hampers its use. Here, we overcome this limitation by combining homozygosity mapping with whole-exome resequencing in a sibling pair with an NPHP-related ciliopathy. Whole-exome capture revealed a homozygous splice acceptor site mutation (c.698G>T) in the renal Mg^{2+} transporter *SLC41A1*. This mutation resulted in skipping of exon 6 of *SLC41A1*, resulting in an in-frame deletion of a transmembrane helix. Transfection of cells with wild-type or mutant SLC41A1 revealed that deletion of exon 6 completely blocks the Mg^{2+} transport function of SLC41A1. Furthermore, in normal human kidney tissue, endogenous SLC41A1 specifically localized to renal tubules situated at the corticomedullary boundary, consistent with the region of cystogenesis observed in NPHP and related ciliopathies. Last, morpholino-mediated knockdown of *slc41a1* expression in zebrafish resulted in ventral body curvature, hydrocephalus, and cystic kidneys, similar to the effects of knocking down other NPHP genes. Taken together, these data suggest that defects in the maintenance of renal Mg^{2+} homeostasis may lead to tubular defects that result in a phenotype similar to NPHP.

J Am Soc Nephrol 24: 967–977, 2013. doi: 10.1681/ASN.2012101034

Rare CKDs make up the majority of CKD cases treated within long-term dialysis and renal transplantation programs in the first three decades of life but are notoriously difficult to diagnose.[1] Rare recessive mutations cause chronic diseases that often require hospitalization.[2] However, half of their single-gene causes are still unknown (http://omim.org/statistics/entries). Because recessive single-gene mutations directly represent the disease cause,

Received October 29, 2012. Accepted February 22, 2013.

T.W.H. and E.A.O. contributed equally to this work.

Published online ahead of print. Publication date available at www.jasn.org.

Correspondence: Dr. Friedhelm Hildebrandt, 8220C MSRBIII, 1150 West Medical Center Drive, Ann Arbor, MI 48109-5646. Email: fhilde@umich.edu

gene identification offers a powerful approach to revealing disease mechanisms. Furthermore, because recessive mutations predominantly convey loss of function, recessive single-gene defects can be transferred directly into animal models to study the related disease mechanisms and to screen for small molecules as possible treatment modalities.

Nephronophthisis (NPHP), a recessive cystic kidney disease, is the most frequent genetic cause of CKD in the first three decades of life. NPHP-related disorders are recessive single-gene disorders that affect kidney, retina, brain, and liver by prenatal-onset dysplasia or by organ degeneration and fibrosis in early adulthood.[3] On ultrasonography, these conditions are characterized by increased echogenicity and cyst formation at the corticomedullary junction in small or normal-sized kidneys.[4] Renal histology exhibits a characteristic triad of renal corticomedullary cysts, tubular basement membrane disruption, and tubulointerstitial infiltrations.[5] Regarding renal, retinal, and hepatic involvement, there is phenotypic overlap of NPHP-related disorders with Bardet-Biedl syndrome and Alstrom syndrome.[6] Identification of recessive mutations in 15 different genes (*NPHP1–NPHP15*)[7–18] revealed that the encoded proteins share localization at the primary cilia-centrosomes complex, which characterizes them as ciliopathies.[3,19] However, the 15 known *NPHP* genes explain less than 50% of all cases with NPHP-related disorders, indicating that many of the single-gene causes of these conditions are still elusive.[20]

The finding that some of the more recently identified genetic causes of NPHP-related disorders are exceedingly rare necessitates a strategy to identify novel single-gene causes of these conditions in single affected families.[15] In this context, the new method of whole exome capture with consecutive massively parallel sequencing (here called whole exome resequencing [WER]) theoretically offers a powerful approach toward gene identification in rare recessive diseases. However, the utility of WER is hampered by the large number of novel genetic variants that result from whole exome sequencing in any given individual.[18,21] To overcome this limitation of WER, we developed a strategy that combines WER with homozygosity mapping.[18] Using this approach, we have identified mutation of the renal magnesium transporter gene *SLC41A1* as a novel genetic cause of disease that phenocopies NPHP-related conditions clinically, ultrasonographically, and histologically.

RESULTS

Identification of Mutation of *SLC41A1* in Family F438

To identify additional causative mutations for NPHP-related disorders, we performed WER in a consanguineous Italian family (F438) with an apparent NPHP-related disorder phenotype (Figure 1A). In this large family, two siblings born from first cousins (IV1 and IV2) displayed the unusual association of apparent NPHP with bronchiectasis.

Patient IV2 had had frequent episodes of fever, coughing, and respiratory infections since the first month of life, and chest radiography demonstrated the persistence of inflammatory infiltrates in the lung. High-resolution computerized tomography revealed bronchiectasis, and fiberoptic bronchoscopy showed reddening of the bronchial mucosa with purulent secretion. Evaluation of bronchoalveolar lavage showed a marked increase in the percentage of neutrophils and the presence of *Pseudomonas aeruginosa*. At age 8 years, the patient was referred to the Nephrology Department because of observed polyuria and polydipsia. Initial urine analysis revealed low urine osmolarity (380 mOsmol/kg in fresh morning urine), and blood analysis displayed renal insufficiency with serum creatinine levels of 2.37 mg/dl. Renal ultrasonography showed bilateral irregular echogenicity, with both kidneys decreased in size (Figure 1B). Percutaneous renal biopsy showed periglomerular fibrosis, tubular ectasia, tubular basement membrane disruption, and tubulointerstitial infiltrations (Figure 1C). On the basis of these clinical findings, a diagnosis of NPHP was proposed. The patient underwent peritoneal dialysis at age 9 years before undergoing kidney transplantation at age 10.

Patient IV1, like his sibling, had had a history of fever, coughing, and respiratory infections since the first month of life. IV1 also presented with polyuria and polydipsia with low urine osmolarity (420 mOsmol/kg) and serum creatinine level of 1.5 mg/dl at 5 years of age. Renal biopsy and renal ultrasonography showed similar findings as for patient IV2 (Figure 1B). Progression of renal damage led to ESRD at age 10 and initiation of peritoneal dialysis.

Patient IV3 is a first-line cousin of siblings IV1 and IV2. She presented with chronic bronchitis and bronchiectasis at age 6 years. However, by age 11 no signs of polyuria or polydipsia were present and results of blood and urine analysis were normal. In addition, renal ultrasonography revealed no abnormalities in kidney size or structure.

Homozygosity mapping performed on patient IV1 yielded eight homozygosity peaks (Figure 2A). By WER, we detected four homozygous variants (Supplemental Table 1) whose segregation pattern fit a recessive mode of inheritance. Of these four variants, only the variant in the *SLC41A1* gene was not a known single-nucleotide polymorphism (SNP) and was absent from both the 1000 Genomes and Exome Variant Server databases (Supplemental Table 2). Furthermore, only the *SLC41A1* variant was predicted to be damaging by all four predictive tools used (Polyphen 1, Polyphen 2, MutationTaster, SIFT [Supplemental Table 2]). In addition, only two of the variants (*SLC41A1* and *ZNF224*) display strong evolutionary conservation at the mutated residue (Supplemental Table 3). Finally, the homozygous missense mutation (c.698G>T, p.G223V) in *SLC41A1* resides within an evolutionary conserved exonic splice acceptor site in exon 6 of *SLC41A1*, probably resulting in missplicing of the *SLC41A1* transcript and thus a potentially more deleterious mutation. This mutation was absent from 100 European-American healthy controls and also absent from 80 regionally matched healthy controls (G. Caridi, personal communication). These

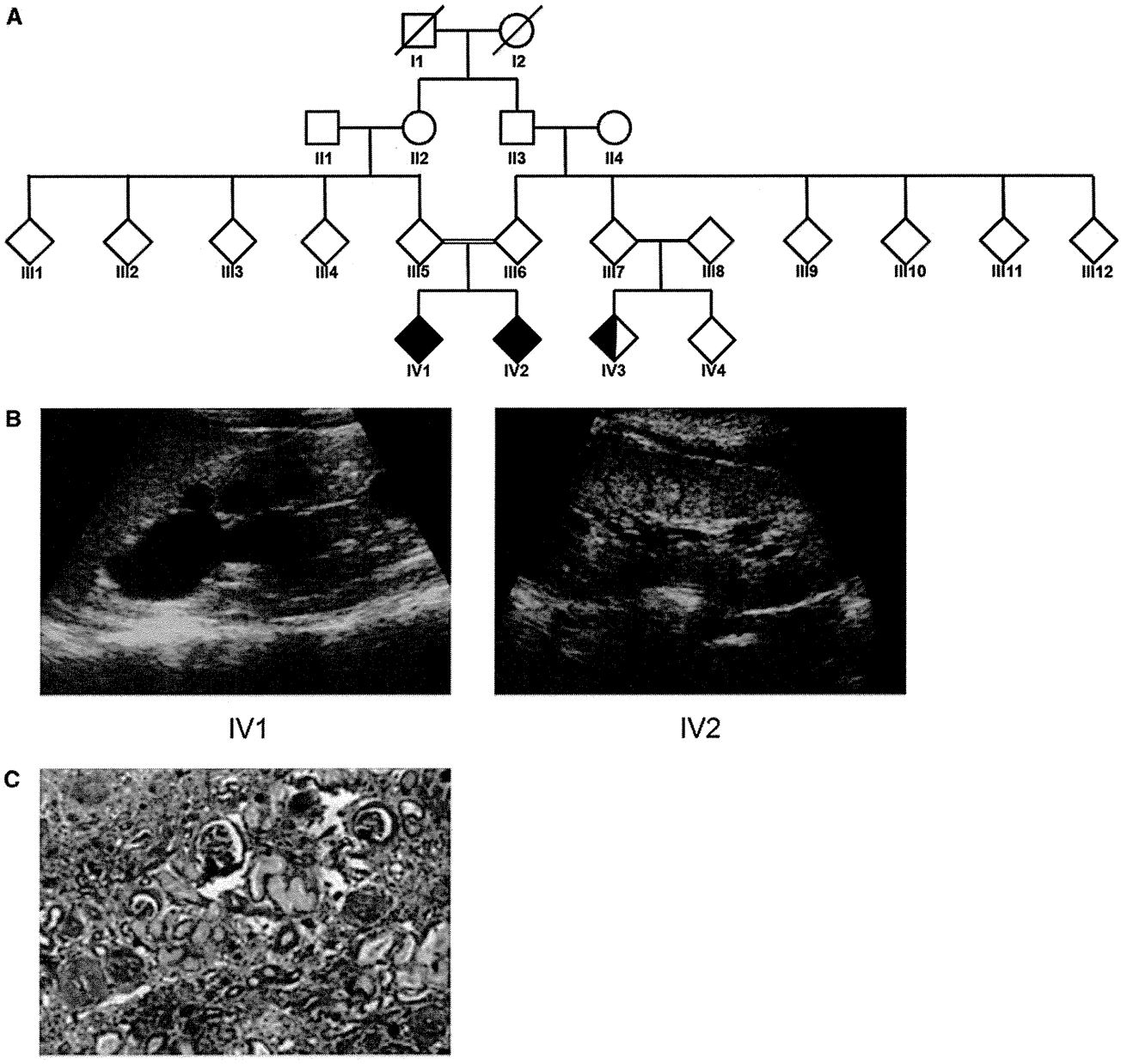

Figure 1. Renal ultrasonography and biopsy indicate characteristic hallmarks of nephronophthisis. (A) Pedigree for family F438. Individuals IV1 and IV2 display both NPHP and primary ciliary dyskinesia (shaded shapes). Individual IV3 has only primary ciliary dyskinesia (half-shaded). (B) RUS showing increased echogenicity, corticomedullary cysts, and loss of corticomedullary differentiation in patients F438-IV1 (left panel) and F438-IV2 (right panel). (C) Renal histologic findings from a renal biopsy specimen from F438-IV1 showing the characteristic triad of tubular ectasia, tubular basement membrane disruption, and tubulointerstitial infiltrations (Trichrome-Masson staining).

data together suggest that *SLC41A1* as a novel causative gene of an NPHP-related disorder phenotype (Figure 2, B and C).

SLC41A1 c.698G>T Mutation Results in Skipping of Exon 6

To test whether the c.698G>T mutation impairs normal splicing of the *SLC41A1* transcript, Epstein Barr virus (EBV)–transformed white blood cells were prepared from blood samples from both parents (III5 and III6) and the two affected siblings (IV1 and IV2). RT-PCR was performed using primers flanking exon 6 (Figure 2B) on cDNA prepared from both the EBV-transformed white blood cells. This test revealed that in both parents, one PCR product of the expected size and an additional faster-migrating PCR product was observed (Figure 2D, upper panel), consistent with the fact that both parents are heterozygous for the c.698G>T mutation. In contrast, RT-PCR on patient-derived cDNA yielded only the single faster-migrating band (Figure 2D, upper panel). Sanger sequencing

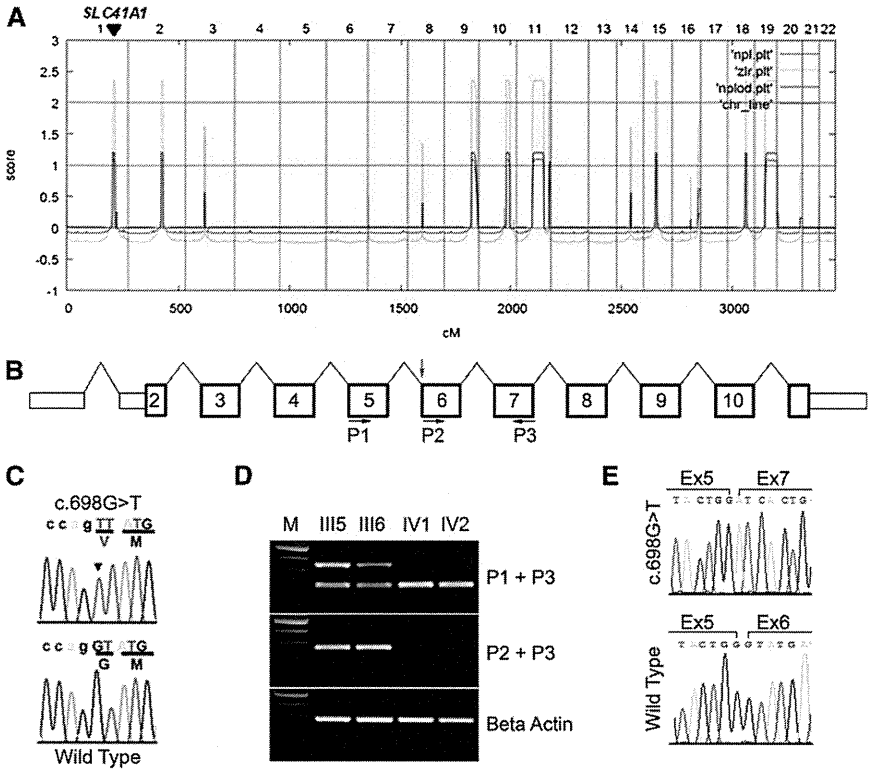

Figure 2. Recessive mutation in *SLC41A1* in family F438 identified by whole exome capture and homozygosity mapping. (A) Homozygosity profile for patient IV1. Nonparametric logarithm of odds scores were plotted over genetic distance across the genome, where chromosomal positions are concatenated from p- to q-arm (left to right). Arrowhead shows the *SLC41A1* locus. (B) Diagram of the human *SLC41A1* gene showing exon number and primer locations. Red arrow shows position of the c.698G>T splice acceptor site mutation. (C) Sanger-sequencing confirmation of the c.698G>T mutation in *SLC41A1*. Altered nucleotide and amino acid change are given above the sequence trace. WT control sequence and trace are shown below the mutated sequence. Codon triplets are underlined to indicate reading frame. Noncoding sequence is in lower case. Mutated nucleotide is denoted by arrowhead. (D) RT-PCR was performed on RNA from lymphoblastoid cells prepared from parents (III5 and III6) and affected siblings (IV1 and IV2) using the primers indicated. Positions of primers is indicated in B. M, 100-bp DNA ladder. (E) Sanger sequencing of the fast and slow migrating RT-PCR products (primers P1 + P3) revealed that the c.698G>T mutation results in skipping of exon 6 (upper trace).

of this faster-migrating band revealed that it arises from skipping of *SLC41A1* exon6 (Figure 2E). Consistent with this observation, further RT-PCR using a forward primer designed against exon 6 (P2; Figure 2B), revealed no detectable PCR product in the two affected siblings but did show a PCR product of the expected size in the two parents (Figure 2D, middle panel). Together, these data demonstrate that the c.698G>T mutation results in missplicing of the *SLC41A1* transcript.

SLC41A1 c.698G>T Mutation Results in Abrogated Protein Expression

The *SLC41A1* mutations that results in skipping of exon 6 is predicted to result in an in-frame deletion of a transmembrane domain. We next tested whether this deletion abrogates expression of SLC41A1. Western blotting of protein lysates generated from both parental and patient-derived cell lines revealed almost complete loss of SLC41A1 expression in the two affected siblings (Figure 3A).

Mutant SLC41A1 Traffics to Cell Surface

We next tested whether the mutated form of SLC41A1 can traffic in a similar fashion as the WT protein. An amino-terminal enhanced green fluorescent protein (EGFP)–tagged SLC41A1 expression construct was generated by cloning the full-length (WT) human SLC41A1 open-reading frame into a mammalian expression vector. In addition, an expression construct with the residues encoded by *SLC41A1* exon 6 deleted was cloned from patient-derived cDNA (dEx6). Transfection of the WT and mutant constructs into the MDCKII renal epithelial cell line revealed that both targeted to the basolateral membrane and that the mutant localization was indistinguishable from WT (Figure 3B). Furthermore, using a cell-surface biotinylation assay in which HEK293 cells were transfected with WT or mutant (dEx6) FLAG-tagged SLC41A1, neutravidin pulldown revealed that both the WT and mutant SLC41A1 are trafficked to the cell surface (Figure 3C). These data suggest that the in-frame deletion of exon 6 does not affect the normal trafficking of SLC41A1.

Deletion of *SLC41A1* Exon 6 Results in Loss of Magnesium Transport Activity of SLC41A1

Because the in-frame deletion of exon6 did not appear to perturb the normal trafficking of SLC41A1, we next sought to address whether the magnesium-transporting ability of SLC41A1 might be compromised by this deletion. In cells transfected with WT SLC41A1, basal free intracellular Mg^{2+} ($[Mg^{2+}]_i$) was, on average, 1.12±0.06 mM (n=20), which was significantly higher than that of mock transfected cells (0.81±0.02 mM, n=20). The average basal $[Mg^{2+}]_i$ of mutant transfected (ΔE6) cells, 0.87±0.04 (n=33), was very similar to that of mock cells (Figure 3D). To examine the Mg^{2+} transport activity, cells were exposed to high Mg^{2+}, low Na^+ solution (Mg^{2+} influx). A 15-minute exposure to high Mg^{2+}, low Na^+ solution resulted in a robust elevation of $[Mg^{2+}]_i$ in WT cells, whereas only small increases in $[Mg^{2+}]_i$ were observed in mock and ΔE6 cells

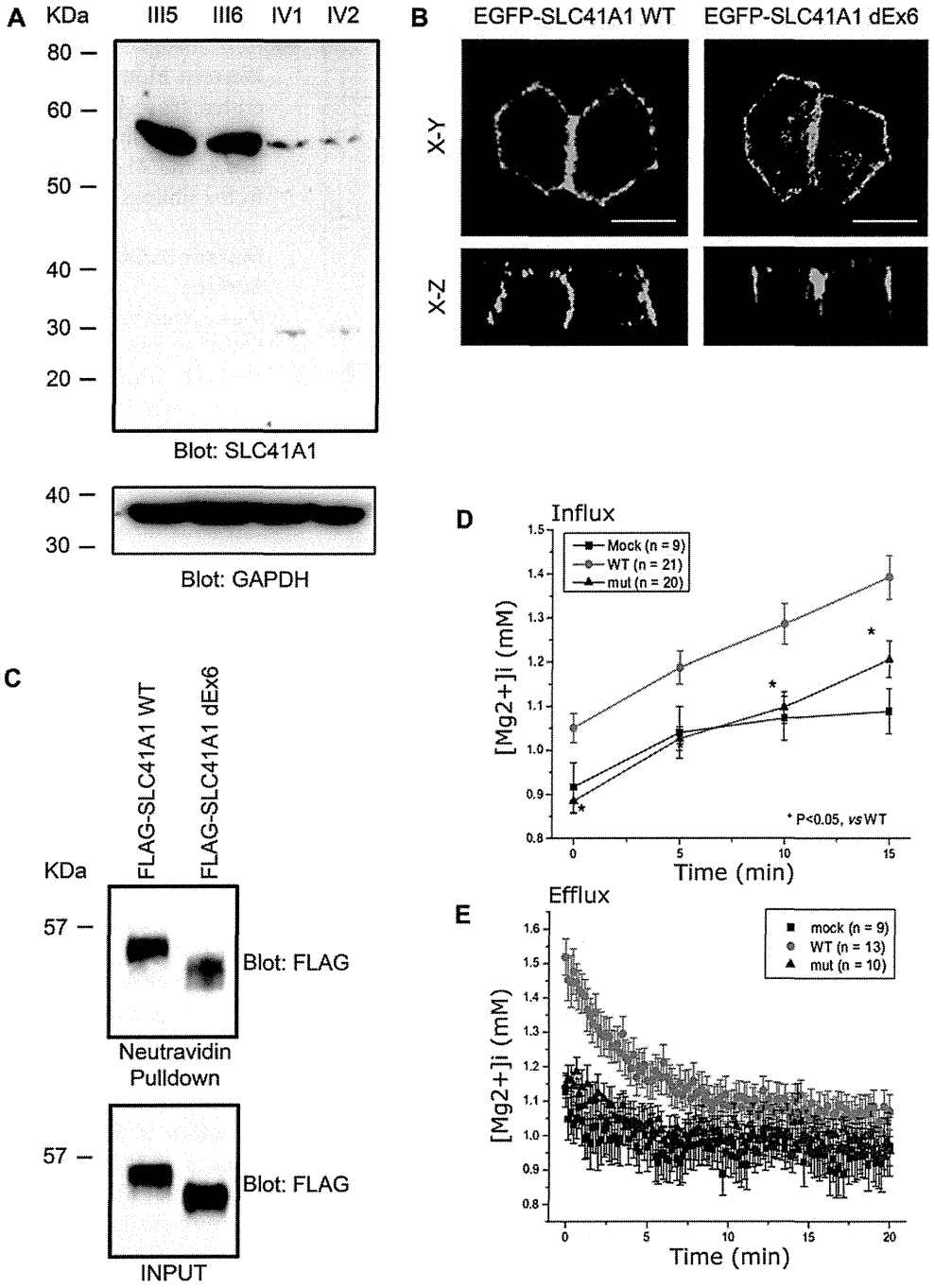

Figure 3. The c.698G>T mutation results in reduced expression and loss of function of SLC41A1. (A) Western blot of lysates prepared from parents (III5 and III6) and affected siblings (IV1 and IV2) showing decreased expression of SLC41A1 in affected siblings. Anti–glyceraldehyde 3-phosphate dehydrogenase (GAPDH) Western blot was used as loading control. (B) EGFP-tagged WT SLC41A1 and SLC41A1 lacking exon 6 (dEx6) were transiently transfected into MDCKII cells. Cells were fixed and EGFP fluorescence captured by confocal microscopy. (C) HEK293 cells transiently transfected with WT or dEx6 FLAG-tagged SLC41A1 were biotinylated at the cell surface before lysis. Cell lysates were then subjected to pulldown with neutravidin beads before SDS-PAGE and Western blotting with the indicated antibodies. (D) HEK293 cells were transfected with empty vector (MOCK) WT or dEx6 EGFP-SLC41A1 before loading with mag-fura2-AM. To measure magnesium influx, cells were exposed to high Mg^{2+}, low Na^{+} solution, and radiometric fluorescent images were collected to determine intracellular [Mg^{2+}]. (E) To measure magnesium efflux, cells were treated as above and then switched into magnesium-free media, and radiometric fluorescent images were collected to determine intracellular [Mg^{2+}]. Error bars show standard deviation.

(WT, 0.50±0.03 μM/s; mock, 0.21±0.04 μM/s; ΔE6, 0.20±0.01 μM/s). When the extracellular solution was switched to the Ca^{2+}-free Tyrode solution, $[Mg^{2+}]_i$ returned to the basal level in WT, ΔE6, and mock cells (Mg^{2+} efflux). Again, Mg^{2+} efflux rates were similar in mock cells and ΔE6 cells (Figure 3E). (Comparison of the efflux rates between WT cells and others is difficult because Mg^{2+} efflux was induced at much higher initial $[Mg^{2+}]_i$ in WT cells.) These data indicate that WT has Mg^{2+} transport activities, whereas ΔE6 mutant has null function.

Localization of SLC41A1 in Kidney

One of the hallmarks or NPHP is the formation of renal cortico-medullary cysts.[3,22] To ascertain why loss of SLC41A1 activity may cause the appearance of cysts at the cortico-medullary boundary, we examined whether *SLC41A1* is expressed in nephron segments in this region. Indeed, immunohistochemical analysis of *SLC41A1* expression on normal human kidney sections revealed expression primarily in the distal convoluted tubules (DCTs) and in the tubule adjacent to the macula densa (Figure 4A). Of note, claudin16, a major regulator of renal paracellular magnesium uptake in which recessive mutations cause renal disease that closely mimics NPHP in cattle,[23] was coexpressed in identical tubular segments to SLC41A1 in rat kidney sections (Figure 4B). In previous studies, RT-PCR has shown that claudin16 is expressed primarily in the DCTs and thick ascending limb of nephrons,[22] and indeed RT-PCR confirmed that *SLC41A1* is also expressed in the DCT and thick ascending limb but is absent from proximal convoluted tubule and cortical collecting duct of microdissected tubular segments (Figure 4C). Together, these data reveal that *SLC41A1* is expressed in the DCT, macula densa, and thick ascending limb tubular segments, whose location is entirely consistent with the region of cystogenesis observed in NPHP and related ciliopathies.

Knockdown of *slc41a1* in Zebrafish Results in Renal Cysts

To confirm that defective SLC41A1 function can lead to cystogenesis, we examined SLC41A1 function in the zebrafish, a widely used model organism for the study of human ciliopathies. Alignment of the human SLC41A1 protein with the zebrafish homolog revealed extensive conservation with 76% identity at the protein level, suggesting that the zebrafish homolog is likely to function in a manner similar to that of human protein (Supplemental Figure 1). To examine the expression pattern of *slc41a1* in zebrafish, an antisense *in situ* probe was generated. By *in situ* hybridization, *slc41a1* was expressed almost exclusively in the corpuscle of Stannius of the zebrafish pronephros, as previously described[24] (Figure 5A). To ablate *slc41a1* expression, a splice-blocking morpholino designed against the splice acceptor site of exon 4 (Figure 5B) was injected into 1–2 cell stage zebrafish embryos. Twenty-four hours after injection, embryos were harvested and the efficacy of the morpholino was examined by RT-PCR. RT-PCR of RNA prepared from embryos injected with a standard control morpholino revealed a PCR product of the expected size, whereas embryos injected with the splice-blocking morpholino exhibited a faster-migrating product indicative of missplicing consistent with skipping of exon 4 (Figure 5C).

To examine the effect of loss of *slc41a1* expression, 48 hours after morpholino injection, the morphology of control and *slc41a1* morphants was examined. Control morphants examined no obvious phenotype, whereas *slc41a1* morphants displayed severe developmental abnormalities (Figure 5, D and E). Specifically, >70% of *slc41a1* morphants exhibited severe ventral body curvature, a phenotype frequently observed upon knockdown of NPHP genes, compared with <2% of embryos injected with the control morpholino (Figure 5D and Supplemental Table 4). In addition, a high proportion (>50%) of the *slc41a1* morphants displayed severe hydrocephalus compared with control morphants (Figure 5D). Morphologic analysis of sections through the hindbrain of *slc41a1* morphants showed extensive dilation of the ventricle compared with controls (Figure 5E).

Because loss of *SLC41A1* function probably leads to renal dysfunction in humans, the presence of pronephric cysts in *slc41a1* morphants was examined. At 56 hours after injection, cross-sections through the zebrafish pronephros revealed the formation of cysts characterized by dilation of the pronephric duct in 60% of *slc41a1* morphants (Figure 5F and Supplemental Table 4). These data reveal that loss of *slc41a1* expression in zebrafish results in renal cyst formation but also several other phenotypes observed upon knockdown of other NPHP genes.[18,25]

DISCUSSION

NPHP-related disorders (including Bardet Biedl, Joubert, Senior-Loken, and Meckel syndromes) display significant locus heterogeneity, with causative mutations occurring in more than 30 different genes. Causative mutation frequency among these genes is not homogenous, ranging from frequent mutations (*NPHP1*, mutated in about 20% of all cases of NPHP-related disorders in our cohort) to extremely rare mutations (*GLIS2/NPHP7*, mutated in a single family).[15,26] It would appear that mutation of *SLC41A1* represents an extremely rare cause of NPHP-related disorders similar to *GLIS2/NPHP7*, as screening of 1000 patients with NPHP-related disorders using a newly developed high-throughput sequencing technique failed to identify any additional patients with *SLC41A1* mutations.[27] Furthermore, it is likely that the identified splice site mutation in *SLC41A1*, resulting in the skipping of exon 6, may be hypomorphic because a small amount of protein product was still detectable in the two affected patients (Figure 3A). Consequently, one may postulate that null mutations resulting from nonsense mutations or deletions might be embryonic lethal and hence not be represented in our cohort of patients with NPHP-RC.

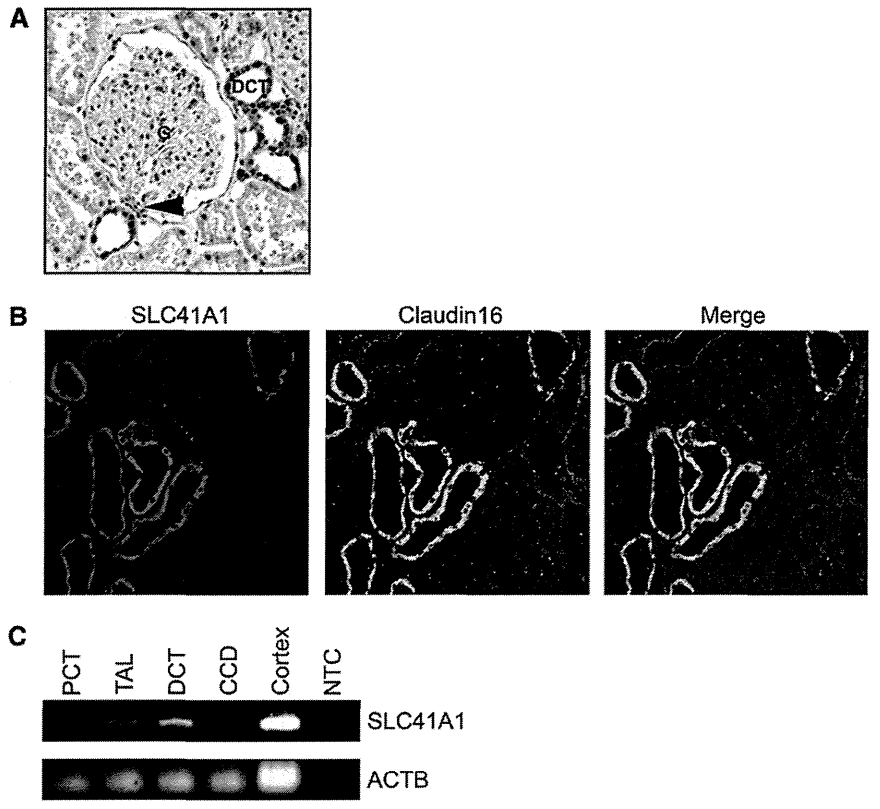

Figure 4. SLC41A1 localizes predominantly to distal convoluted tubules. (A) Immunohistochemistry was performed on human paraffin-embedded sections using rabbit anti-SLC41A1 antibodies. Signal was seen primarily in the DCTs. G, glomerulus. Arrowhead shows macula densa. (B) Rat paraffin-embedded sections were immunostained with antibodies against SLC41A1 (red) and Claudin 16 (green). DAPI (blue) was used to stain cell nuclei. (C) RT-PCR was performed on human nephron segments with primers for SLC41A1 and actin-β (ACTB) as loading control. CCD, cortical collecting duct; NTC, no template control; PCT, proximal convoluted tubule; TAL, thick ascending limb.

What remains to be ascertained in this case is the cause of the bronchiectasis in the two affected siblings and their cousin. The identified mutation in *SLC41A1* can explain the renal phenotype of the two affected siblings but cannot explain the cause of bronchiectasis because the cousin who had lung dysfunction but no renal disease is heterozygous for the *SLC41A1* mutation. A dominant effect for the *SLC41A1* allele is unlikely because neither parent of the two affected siblings who are heterozygous for the mutant *SLC41A1* allele showed any bronchiectasis phenotype. The possibility that the cousin had a compound heterozygous mutation in *SLC41A1* was ruled out as Sanger sequencing of all exons failed to identify additional mutations (data not show). The bronchiectasis phenotype probably arises from mutation of a separate gene. Using our exome data, we searched for mutations in all known primary ciliary dyskinesia genes, and although we did find variations in several, none of them segregated correctly with affected status within the family (Supplemental Table 5). Alternatively, the respiratory problems observed in the cousin (IV3) may be a phenocopy of the disease observed in the two siblings (IV1 and IV2). This is supported by the observation that the two affected siblings displayed symptoms of lung dysfunction soon after birth, whereas the cousin only exhibited problems at age 6 years.

Intracellular Mg^{2+} is a cofactor for enzymes and signal transduction proteins and regulates bioenergetics, ion transport, growth, and proliferation. $[Mg^{2+}]_i$ is thought to be maintained by transport across cell membranes with Mg^{2+} transporters. SLC41A1, a member of the solute carrier family 41, is a cell membrane protein expressed in various tissues, including heart, brain, kidney, liver, and colon, and has been proposed as one of the candidates for such Mg^{2+} transporters.[28–30] Although Mg^{2+} transport by SLC41A1 has not been fully characterized, Kolisek *et al.* recently reported that the human *SLC41A1* gene encodes for the Na^+/Mg^{2+} exchanger 4.[28] The finding that mutations of this renal Mg^{2+} transporter mimics an NPHP-RC phenotype may be related to the fact that other mutations in proteins involved in renal Mg^{2+} transport are known to cause an NPHP-related disorder phenotype. Specifically, recessive mutations of the *CLDN16* gene encoding the renal tight junction protein claudin-16 (also called paracellin-1) cause a recessive renal disease that closely mimics NPHP[31] in cattle[24] both clinically and histologically. An unusual finding, given that SLC41A1 is an apparent magnesium transporter, is that neither of the affected patients exhibited any abnormalities in serum or urine magnesium content or any evidence of nephrocalcinosis (G. Caridi, personal communication). Hence, the disease phenotype may result from perturbed intracellular magnesium homeostasis rather than global alterations in magnesium levels.

It is unclear how loss of correct magnesium homeostasis within the epithelial cells of the distal convoluted tubule could lead to the formation of cysts and the development of the NPHP-related disorder phenotype. Because the majority of cases of NPHP-related disorders are caused by mutations in genes whose products reside at or regulate ciliary function, one possibility is that the SLC41A1 transporter is regulated downstream of the NPHP-protein/ciliary network. Analysis of whether cellular magnesium levels are perturbed upon loss of cilia or knockdown of other NPHP proteins could potentially provide important insight into the pathogenesis of NPHP-related disorders. Of note, SLC41A1 is the first transporter to

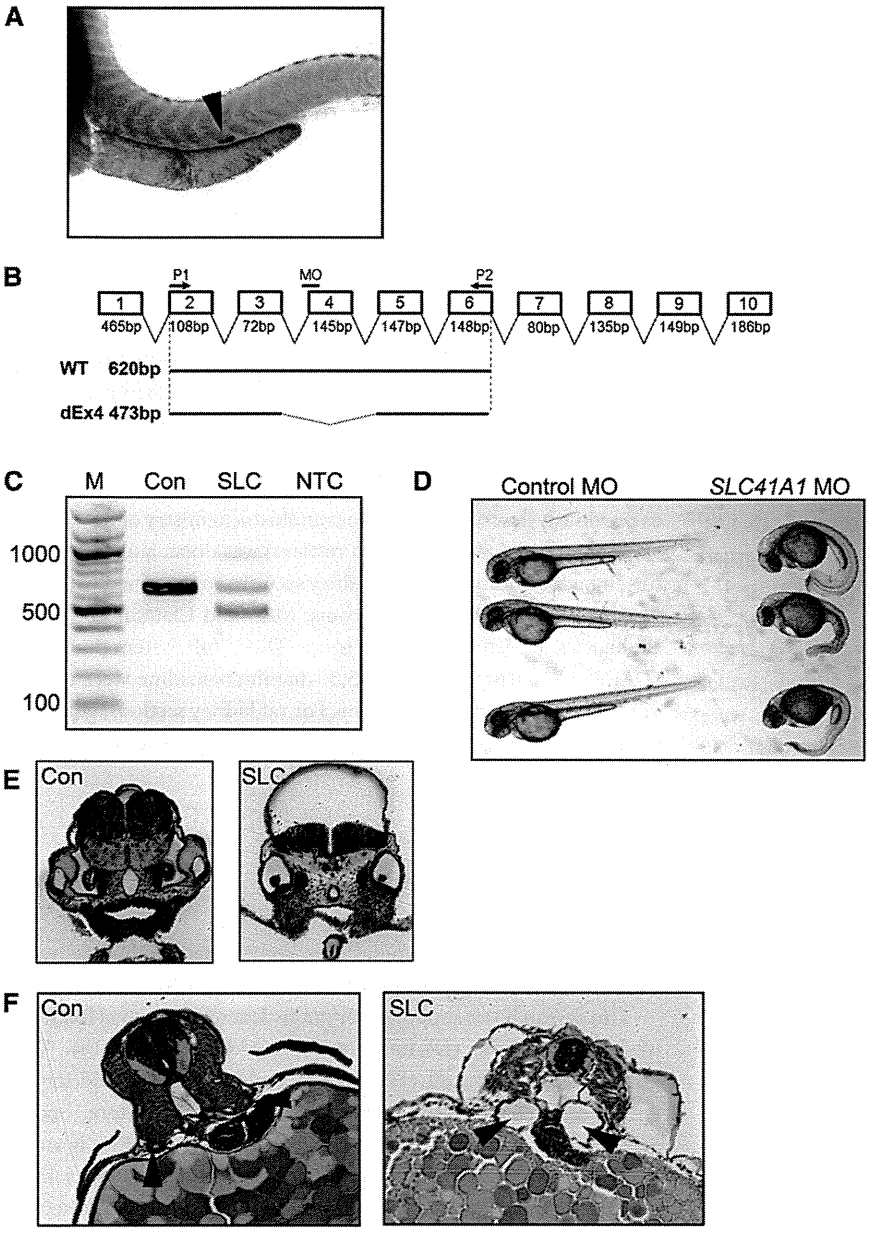

Figure 5. Knockdown of *slc41a1* expression in zebrafish results in kidney cysts. (A) *In situ* hybridization of 48-hour-old zebrafish embryos with an antisense *slc41a1* probe showing expression in the corpuscle of Stannius (arrowhead). (B) Schematic diagram of the zebrafish *slc41a1* gene showing location of the splice-blocking morpholino (MO) and primers used for RT-PCR (P1 and P2). Shown below are expected RT-PCR products using primers P1 and P2 on WT and splice morpholino injected (dEx4) samples and their expected sizes. (C) RT-PCR was performed on RNA prepared from embryos 24 hours after injection with standard control (Con) or *slc41a1* splice-blocking morpholino (SLC). Shown on the left are the sizes (in bp) of the major bands of the DNA ladder (M). NTC, no template control. (D) Phenotypic appearance at 48 hours of control and slc41a1 morpholino–injected embryos. (E) Methylene blue–stained plastic sections showing prominent hydrocephalus in *slc41a1* morpholino–injected embryos (right panel) compared with control morpholino–injected embryos (left panel). (F) Methylene blue–stained plastic sections showing tubular dilation (cysts) in *slc41a1* morpholino–injected embryos (right panel) compared with control morpholino–injected embryos (left panel). Arrowheads show pronephric tubules.

be identified as causing an NPHP-related disorder, and as such it represents an attractive potential target for pharmacologic intervention for the treatment of these disorders.

CONCISE METHODS

Research Participants

From worldwide sources we obtained blood samples and clinical and pedigree data after individuals with NPHP-related disorders and/or their parents provided informed consent. Approval for human subjects' research was obtained from the University of Michigan Institutional Review Board and relevant local review boards. NPHP-related disorder was diagnosed by (pediatric) nephrologists on the basis of standardized clinical[32] and renal ultrasonographic criteria.[4] Renal biopsy specimens were evaluated by renal pathologists.[5] Clinical data were obtained using a standardized questionnaire (http://www.renalgenes.org). Mutations in selected known *NPHP*-related condition genes were excluded using an approach of high-throughput mutation analysis.[33,34]

Homozygosity Mapping

For genome-wide homozygosity mapping[35] the Genome-wide Human SNP 6.0 ArrayII from Affymetrix was used. Genomic DNA samples were hybridized and scanned using the manufacturer's standard protocol at the University of Michigan Core Facility (www.michiganmicroarray.com). Nonparametric logarithm-of-odds scores were calculated using a modified version of the program GENEHUNTER 2.1[36,37] through stepwise use of a sliding window with sets of 110 SNPs using the program ALLEGRO.[38] Genetic regions of homozygosity by descent (homozygosity peaks) were plotted across the genome as candidate regions for recessive disease-causing genes. Disease allele frequency was set at 0.0001, and Caucasian marker allele frequencies were used.

Whole Exome Sequencing

Exome enrichment was conducted following the manufacturer's protocol for the NimbleGen SeqCap EZ Exome v2 beads (Roche NimbleGen Inc.). The kit interrogates a total of approximately 30,000 genes (about 330,000 consensus coding DNA sequence exons). Massively parallel sequencing was performed largely as described

in Bentley *et al.*[39] Sequence reads were mapped to the human reference genome assembly (National Center for Biotechnology Information build 36/hg18) and mutation calling performed using CLC Genomics Workbench (version 4.7.2) software (CLC bio, Aarhus, Denmark).

Cell Culture

HEK293T and MDCK II cells were cultured in DMEM with 10% FBS in 5% CO_2 at 37°C. Transfection was performed using Lipofectamine 2000 (Invitrogen). Cell surface biotinylation assay was performed with the Cell Surface Protein Isolation kit (Thermo Scientific) according to the manufacturer's protocol.

Constructs

Human SLC41A1 was cloned from human kidney cDNA (Clontech). Exon 6–deleted SLC41A1 was cloned from the cDNA made from EBV-transformed proband's peripheral lymphocytes. SLC41A1 cDNAs were subcloned into pEGFP-C (Invitrogen) or FLAG-tagged pcDNA3.1.

Measurement of Magnesium Influx and Efflux

Transfected cells were grown on 35-mm glass base dishes (Iwaki, Chiba, Japan) coated with Matrigel (BD Biosciences). Cells were washed with Ca^{2+}-free Tyrode solution composed of (in mM): 135 NaCl, 5.4 KCl, 1.0 $MgCl_2$, 0.33 NaH_2PO_4, 0.1 EGTA, 10 HEPES, and 2 glucose (pH 7.4 at 25°C by NaOH). After the background fluorescence of the GFP-positive transfected cells were measured, cells were incubated with 5 μM mag-fura-2-AM for 10 minutes, followed by three washes and further 20-minute incubation in the Ca^{2+}-free Tyrode solution on the stage of inverted microscope (TE300; Nikon, Tokyo, Japan). The fluorescence images of mag-fura-2 were collected from the cells at 25°C by a cooled charge-coupled device system (EM-CCD C9100, Hamamatsu Photonics, Hamamatsu, Japan) with a 40× objective (S fluor 40×0.90, Nikon). With alternate excitation at 345 and 380 nm, mag-fura-2 fluorescence images at wavelength longer than 470 nm were acquired, and digitized data were analyzed with image analysis software (Aquacosmos/Ratio, Hamamatsu Photonics). The ratio of fluorescence intensities excited at 380 nm and 345 nm was calibrated in terms of $[Mg^{2+}]_i$ as described previously.[40] To assess Mg^{2+} influx, cells were exposed to a high Mg^{2+}, low Na^+ solution composed of (in mM): 68.5 $MgCl_2$, 24 Mg-methanesulfonate, 5.4 KCl, 0.33 NaH_2PO_4, 0.1 EGTA, 10 HEPES, and 2 glucose (pH 7.4), and fluorescence images were obtained at 0, 5, 10, and 15 minutes. To assess Mg^{2+} efflux, extracellular solutions of the Mg^{2+}-loaded cells were changed back to the Ca^{2+}-free Tyrode solution and fluorescence images were obtained every 10 seconds for 20 minutes.

Morpholino Oligo-Mediated Knock-Down

To knock down zebrafish *slc41a1*, a splice-site blocking morpholino was designed against the *slc41a1* exon 4 splice acceptor site (TGAACCTGAACACAGCAGAGGGACA). Morpholinos were dissolved in nuclease-free water and injected into zebrafish embryos at 1- to 4-cell stages in 0.1 M KCl at the specified dosage. The injection volume is estimated to be 1–2 nl.

Human Kidney Samples

Kidney cortex tissues were obtained during unilateral nephrectomy for renal carcinoma.[41] The institutional review board of University of Tokyo School of Medicine approved the study. Human nephron segments were obtained from manual microdissection, as described previously.[42] Total RNA isolated from each nephron segments was used for RT-PCR. Primers were 5′-ggtcttcatcctagtgcctg and 5′-caaggtgatgaggtcgcc for SLC41A1; 5′-cgcaaagacctgtacgccaac and 5′-ccacacggagtacttgcgctc for ACTB.

Histology

Zebrafish embryos were fixed with 4% paraformaldehyde overnight, serial-dehydrated with 25%, 50%, 75%, and 95% ethanol, and then equilibrated with JB-4 solution (Polysciences) overnight at 4°C. The embryos were embedded in JB-4 resin and sectioned with a Leica R2265 microtome. The sections were stained with methylene blue as previously described.[25] For immunohistochemistry of human and rat kidney heat-induced antigen retrieval was done, and then paraffin-embedded human and rat kidney sections were stained with anti-SLC41A1 (Sigma Aldrich, St. Louis, MO) and Claudin 16 (Novus Biologicals, Littleton, CO). EnVision+ Dual Link System peroxidase (DAKO, Carpinteria, CA) and 3,3′-diaminobenzidine were used to visualize staining in human tissue. For rat kidney sections, goat anti-mouse A488 and goat antirabbit A594 (Invitrogen) secondary antibodies were used.

ACKNOWLEDGMENTS

The authors thank the families who contributed to this study. We thank Robert H. Lyons for excellent Sanger sequencing.

This research was supported by grants from the National Institutes of Health to F.H. (DK1069274, DK1068306, DK064614), W.Z. (DK091405), and E.A.O. (DK090917), and by a grant-in-aid for scientific research from the Ministry of Education, Culture, Sports, Science, and Technology of Japan to T.A. (23390033). F.H. is an investigator of the Howard Hughes Medical Institute, a Doris Duke Distinguished Clinical Scientist, and a Frederick G.L. Huetwell Professor.

DISCLOSURES

None.

REFERENCES

1. Smith JM, Stablein DM, Munoz R, Hebert D, McDonald RA: Contributions of the Transplant Registry: The 2006 Annual Report of the North American Pediatric Renal Trials and Collaborative Studies (NAPRTCS). *Pediatr Transplant* 11: 366–373, 2007
2. Bell C.J., et al Carrier testing for severe childhood recessive diseases by next-generation sequencing. *Sci Transl Med* 3: 65ra4, 2011.
3. Hildebrandt F, Benzing T, Katsanis N: Ciliopathies. *N Engl J Med* 364: 1533–1543, 2011

4. Blowey DL, Querfeld U, Geary D, Warady BA, Alon U: Ultrasound findings in juvenile nephronophthisis. *Pediatr Nephrol* 10: 22–24, 1996
5. Zollinger HU, Mihatsch MJ, Edefonti A, Gaboardi F, Imbasciati E, Lennert T: Nephronophthisis (medullary cystic disease of the kidney). A study using electron microscopy, immunofluorescence, and a review of the morphological findings. *Helv Paediatr Acta* 35: 509–530, 1980
6. Badano JL, Mitsuma N, Beales PL, Katsanis N: The ciliopathies: An emerging class of human genetic disorders. *Annu Rev Genomics Hum Genet* 7: 125–148, 2006
7. Hildebrandt F, Otto E, Rensing C, Nothwang HG, Vollmer M, Adolphs J, Hanusch H, Brandis M: A novel gene encoding an SH3 domain protein is mutated in nephronophthisis type 1. *Nat Genet* 17: 149–153, 1997
8. Otto EA, Schermer B, Obara T, O'Toole JF, Hiller KS, Mueller AM, Ruf RG, Hoefele J, Beekmann F, Landau D, Foreman JW, Goodship JA, Strachan T, Kispert A, Wolf MT, Gagnadoux MF, Nivet H, Antignac C, Walz G, Drummond IA, Benzing T, Hildebrandt F: Mutations in INVS encoding inversin cause nephronophthisis type 2, linking renal cystic disease to the function of primary cilia and left-right axis determination. *Nat Genet* 34: 413–420, 2003
9. Olbrich H, Fliegauf M, Hoefele J, Kispert A, Otto E, Volz A, Wolf MT, Sasmaz G, Trauer U, Reinhardt R, Sudbrak R, Antignac C, Gretz N, Walz G, Schermer B, Benzing T, Hildebrandt F, Omran H: Mutations in a novel gene, NPHP3, cause adolescent nephronophthisis, tapeto-retinal degeneration and hepatic fibrosis. *Nat Genet* 34: 455–459, 2003
10. Otto E, Hoefele J, Ruf R, Mueller AM, Hiller KS, Wolf MT, Schuermann MJ, Becker A, Birkenhäger R, Sudbrak R, Hennies HC, Nürnberg P, Hildebrandt F: A gene mutated in nephronophthisis and retinitis pigmentosa encodes a novel protein, nephroretinin, conserved in evolution. *Am J Hum Genet* 71: 1161–1167, 2002
11. Mollet G, Salomon R, Gribouval O, Silbermann F, Bacq D, Landthaler G, Milford D, Nayir A, Rizzoni G, Antignac C, Saunier S: The gene mutated in juvenile nephronophthisis type 4 encodes a novel protein that interacts with nephrocystin. *Nat Genet* 32: 300–305, 2002
12. Otto E, Loeys B, Khanna H, Hellemans J, Sudbrak R, Fan S, Muerb U, O'Toole JF, Helou J, Attanasio M, Utsch B, Sayer JA, Lillo C, Jimeno D, Coucke P, De Paepe A, Reinhardt R, Klages S, Tsuda M, Kawakami I, Kusakabe T, Omran H, Imm A, Tippens M, Raymond PA, Hill J, Beales P, He S, Kispert A, Margolis B, Williams DS, Swaroop A, Hildebrandt F: A novel ciliary IQ domain protein, NPHP5, is mutated in Senior-Loken syndrome (nephronophthisis with retinitis pigmentosa), and interacts with RPGR and calmodulin. *Nat Genet* 37: 282–288, 2005
13. Sayer JA, Otto EA, O'Toole JF, Nurnberg G, Kennedy MA, Becker C, Hennies HC, Helou J, Attanasio M, Fausett BV, Utsch B, Khanna H, Liu Y, Drummond I, Kawakami I, Kusakabe T, Tsuda M, Ma L, Lee H, Larson RG, Allen SJ, Wilkinson CJ, Nigg EA, Shou C, Lillo C, Williams DS, Hoppe B, Kemper MJ, Neuhaus T, Parisi MA, Glass IA, Petry M, Kispert A, Gloy J, Ganner A, Walz G, Zhu X, Goldman D, Nurnberg P, Swaroop A, Leroux MR, Hildebrandt F: The centrosomal protein nephrocystin-6 is mutated in Joubert syndrome and activates transcription factor ATF4. *Nat Genet* 38: 674–681, 2006
14. Valente EM, Silhavy JL, Brancati F, Barrano G, Krishnaswami SR, Castori M, Lancaster MA, Boltshauser E, Boccone L, Al-Gazali L, Fazzi E, Signorini S, Louie CM, Bellacchio E, Bertini E, Dallapiccola B, Gleeson JG; International Joubert Syndrome Related Disorders Study Group: Mutations in CEP290, which encodes a centrosomal protein, cause pleiotropic forms of Joubert syndrome. *Nat Genet* 38: 623–625, 2006
15. Attanasio M, Uhlenhaut NH, Sousa VH, O'Toole JF, Otto E, Anlag K, Klugmann C, Treier AC, Helou J, Sayer JA, Seelow D, Nürnberg G, Becker C, Chudley AE, Nürnberg P, Hildebrandt F, Treier M: Loss of GLIS2 causes nephronophthisis in humans and mice by increased apoptosis and fibrosis. *Nat Genet* 39: 1018–1024, 2007
16. Delous M, Baala L, Salomon R, Laclef C, Vierkotten J, Tory K, Golzio C, Lacoste T, Besse L, Ozilou C, Moutkine I, Hellman NE, Anselme I, Silbermann F, Vesque C, Gerhardt C, Rattenberry E, Wolf MT, Gubler MC, Martinovic J, Encha-Razavi F, Boddaert N, Gonzales M, Macher MA, Nivet H, Champion G, Berthélémé JP, Niaudet P, McDonald F, Hildebrandt F, Johnson CA, Vekemans M, Antignac C, Rüther U, Schneider-Maunoury S, Attié-Bitach T, Saunier S: The ciliary gene RPGRIP1L is mutated in cerebello-oculo-renal syndrome (Joubert syndrome type B) and Meckel syndrome. *Nat Genet* 39: 875–881, 2007
17. Otto EA, Trapp ML, Schultheiss UT, Helou J, Quarmby LM, Hildebrandt F: NEK8 mutations affect ciliary and centrosomal localization and may cause nephronophthisis. *J Am Soc Nephrol* 19: 587–592, 2008
18. Otto EA, Hurd TW, Airik R, Chaki M, Zhou W, Stoetzel C, Patil SB, Levy S, Ghosh AK, Murga-Zamalloa CA, van Reeuwijk J, Letteboer SJ, Sang L, Giles RH, Liu Q, Coene KL, Estrada-Cuzcano A, Collin RW, McLaughlin HM, Held S, Kasanuki JM, Ramaswami G, Conte J, Lopez I, Washburn J, Macdonald J, Hu J, Yamashita Y, Maher ER, Guay-Woodford LM, Neumann HP, Obermüller N, Koenekoop RK, Bergmann C, Bei X, Lewis RA, Katsanis N, Lopes V, Williams DS, Lyons RH, Dang CV, Brito DA, Dias MB, Zhang X, Cavalcoli JD, Nürnberg G, Nürnberg P, Pierce EA, Jackson PK, Antignac C, Saunier S, Roepman R, Dollfus H, Khanna H, Hildebrandt F: Candidate exome capture identifies mutation of SDCCAG8 as the cause of a retinal-renal ciliopathy. *Nat Genet* 42: 840–850, 2010
19. Ansley SJ, Badano JL, Blacque OE, Hill J, Hoskins BE, Leitch CC, Kim JC, Ross AJ, Eichers ER, Teslovich TM, Mah AK, Johnsen RC, Cavender JC, Lewis RA, Leroux MR, Beales PL, Katsanis N: Basal body dysfunction is a likely cause of pleiotropic Bardet-Biedl syndrome. *Nature* 425: 628–633, 2003
20. Otto EA, Ramaswami G, Janssen S, Chaki M, Allen SJ, Zhou W, Airik R, Hurd TW, Ghosh AK, Wolf MT, Hoppe B, Neuhaus TJ, Bockenhauer D, Milford DV, Soliman NA, Antignac C, Saunier S, Johnson CA, Hildebrandt F; GPN Study Group: Mutation analysis of 18 nephronophthisis associated ciliopathy disease genes using a DNA pooling and next generation sequencing strategy. *J Med Genet* 48: 105–116, 2011
21. Ng SB, Turner EH, Robertson PD, Flygare SD, Bigham AW, Lee C, Shaffer T, Wong M, Bhattacharjee A, Eichler EE, Bamshad M, Nickerson DA, Shendure J: Targeted capture and massively parallel sequencing of 12 human exomes. *Nature* 461: 272–276, 2009
22. Efrati E, Arsentiev-Rozenfeld J, Zelikovic I: The human paracellin-1 gene (hPCLN-1): Renal epithelial cell-specific expression and regulation. *Am J Physiol Renal Physiol* 288: F272–F283, 2005
23. Ohba Y, Kitagawa H, Kitoh K, Sasaki Y, Takami M, Shinkai Y, Kunieda T: A deletion of the paracellin-1 gene is responsible for renal tubular dysplasia in cattle. *Genomics* 68: 229–236, 2000
24. Wingert RA, Davidson AJ: The zebrafish pronephros: A model to study nephron segmentation. *Kidney Int* 73: 1120–1127, 2008
25. Zhou W, Dai J, Attanasio M, Hildebrandt F: Nephrocystin-3 is required for ciliary function in zebrafish embryos. *Am J Physiol Renal Physiol* 299: F55–F62, 2010
26. Soliman NA, Hildebrandt F, Otto EA, Nabhan MM, Allen SJ, Badr AM, Sheba M, Fadda S, Gawdat G, El-Kiky H: Clinical characterization and NPHP1 mutations in nephronophthisis and associated ciliopathies: Asingle center experience. *Saudi J Kidney Dis Transpl* 23: 1090–1098, 2012
27. Halbritter J, Diaz K, Chaki M, Porath JD, Tarrier B, Fu C, Innis JL, Allen SJ, Lyons RH, Stefanidis CJ, Omran H, Soliman NA, Otto EA: High-throughput mutation analysis in patients with a nephronophthisis-associated ciliopathy applying multiplexed barcoded array-based PCR amplification and next-generation sequencing. *J Med Genet* 49: 756–767, 2012
28. Kolisek M, Nestler A, Vormann J, Schweigel-Röntgen M: Human gene SLC41A1 encodes for the Na+/Mg^{2+} exchanger. *Am J Physiol Cell Physiol* 302: C318–C326, 2012
29. Goytain A, Quamme GA: Functional characterization of human SLC41A1, a Mg2+ transporter with similarity to prokaryotic MgtE Mg2+ transporters. *Physiol Genomics* 21: 337–342, 2005

30. Mandt T, Song Y, Scharenberg AM, Sahni J: SLC41A1 Mg(2+) transport is regulated via Mg(2+)-dependent endosomal recycling through its N-terminal cytoplasmic domain. *Biochem J* 439: 129–139, 2011
31. Simon DB, Lu Y, Choate KA, Velazquez H, Al-Sabban E, Praga M, Casari G, Bettinelli A, Colussi G, Rodriguez-Soriano J, McCredie D, Milford D, Sanjad S, Lifton RP: *Paracellin-1, a renal tight junction protein required* for paracellular Mg2+ resorption. *Science* 285: 103–106, 1999
32. Waldherr R, Lennert T, Weber HP, Födisch HJ, Schärer K: The nephronophthisis complex. A clinicopathologic study in children. *Virchows Arch A Pathol Anat Histol* 394: 235–254, 1982
33. Otto EA, et al: Mutation analysis of 18 nephronophthisis associated ciliopathy disease genes using a DNA pooling and next generation sequencing strategy. *J Med Genet* 48: 105–116, 2011
34. Harville HM, Held S, Diaz-Font A, Davis EE, Diplas BH, Lewis RA, Borochowitz ZU, Zhou W, Chaki M, MacDonald J, Kayserili H, Beales PL, Katsanis N, Otto E, Hildebrandt F: Identification of 11 novel mutations in eight BBS genes by high-resolution homozygosity mapping. *J Med Genet* 47: 262–267, 2010
35. Hildebrandt F, Heeringa SF, Rüschendorf F, Attanasio M, Nürnberg G, Becker C, Seelow D, Huebner N, Chernin G, Vlangos CN, Zhou W, O'Toole JF, Hoskins BE, Wolf MT, Hinkes BG, Chaib H, Ashraf S, Schoeb DS, Ovunc B, Allen SJ, Vega-Warner V, Wise E, Harville HM, Lyons RH, Washburn J, Macdonald J, Nürnberg P, Otto EA: A systematic approach to mapping recessive disease genes in individuals from outbred populations. *PLoS Genet* 5: e1000353, 2009
36. Strauch K, Fimmers R, Kurz T, Deichmann KA, Wienker TF, Baur MP: Parametric and nonparametric multipoint linkage analysis with imprinting and two-locus-trait models: Application to mite sensitization. *Am J Hum Genet* 66: 1945–1957, 2000
37. Kruglyak L, Daly MJ, Reeve-Daly MP, Lander ES: Parametric and nonparametric linkage analysis: Aunified multipoint approach. *Am J Hum Genet* 58: 1347–1363, 1996
38. Gudbjartsson DF, Jonasson K, Frigge ML, Kong A: Allegro, a new computer program for multipoint linkage analysis. *Nat Genet* 25: 12–13, 2000
39. Bentley DR, Balasubramanian S, Swerdlow HP, Smith GP, Milton J, Brown CG, Hall KP, Evers DJ, Barnes CL, Bignell HR, Boutell JM, Bryant J, Carter RJ, Keira Cheetham R, Cox AJ, Ellis DJ, Flatbush MR, Gormley NA, Humphray SJ, Irving LJ, Karbelashvili MS, Kirk SM, Li H, Liu X, Maisinger KS, Murray LJ, Obradovic B, Ost T, Parkinson ML, Pratt MR, Rasolonjatovo IM, Reed MT, Rigatti R, Rodighiero C, Ross MT, Sabot A, Sankar SV, Scally A, Schroth GP, Smith ME, Smith VP, Spiridou A, Torrance PE, Tzonev SS, Vermaas EH, Walter K, Wu X, Zhang L, Alam MD, Anastasi C, Aniebo IC, Bailey DM, Bancarz IR, Banerjee S, Barbour SG, Baybayan PA, Benoit VA, Benson KF, Bevis C, Black PJ, Boodhun A, Brennan JS, Bridgham JA, Brown RC, Brown AA, Buermann DH, Bundu AA, Burrows JC, Carter NP, Castillo N, Chiara E Catenazzi M, Chang S, Neil Cooley R, Crake NR, Dada OO, Diakoumakos KD, Dominguez-Fernandez B, Earnshaw DJ, Egbujor UC, Elmore DW, Etchin SS, Ewan MR, Fedurco M, Fraser LJ, Fuentes Fajardo KV, Scott Furey W, George D, Gietzen KJ, Goddard CP, Golda GS, Granieri PA, Green DE, Gustafson DL, Hansen NF, Harnish K, Haudenschild CD, Heyer NI, Hims MM, Ho JT, Horgan AM, Hoschler K, Hurwitz S, Ivanov DV, Johnson MQ, James T, Huw Jones TA, Kang GD, Kerelska TH, Kersey AD, Khrebtukova I, Kindwall AP, Kingsbury Z, Kokko-Gonzales PI, Kumar A, Laurent MA, Lawley CT, Lee SE, Lee X, Liao AK, Loch JA, Lok M, Luo S, Mammen RM, Martin JW, McCauley PG, McNitt P, Mehta P, Moon KW, Mullens JW, Newington T, Ning Z, Ling Ng B, Novo SM, O'Neill MJ, Osborne MA, Osnowski A, Ostadan O, Paraschos LL, Pickering L, Pike AC, Pike AC, Chris Pinkard D, Pliskin DP, Podhasky J, Quijano VJ, Raczy C, Rae VH, Rawlings SR, Chiva Rodriguez A, Roe PM, Rogers J, Rogert Bacigalupo MC, Romanov N, Romieu A, Roth RK, Rourke NJ, Ruediger ST, Rusman E, Sanches-Kuiper RM, Schenker MR, Seoane JM, Shaw RJ, Shiver MK, Short SW, Sizto NL, Sluis JP, Smith MA, Ernest Sohna Sohna J, Spence EJ, Stevens K, Sutton N, Szajkowski L, Tregidgo CL, Turcatti G, Vandevondele S, Verhovsky Y, Virk SM, Wakelin S, Walcott GC, Wang J, Worsley GJ, Yan J, Yau L, Zuerlein M, Rogers J, Mullikin JC, Hurles ME, McCooke NJ, West JS, Oaks FL, Lundberg PL, Klenerman D, Durbin R, Smith AJ: Accurate whole human genome sequencing using reversible terminator chemistry. *Nature* 456: 53–59, 2008
40. Tashiro M, Inoue H, Konishi M: KB-R7943 inhibits Na+-dependent Mg2+ efflux in rat ventricular myocytes. *J Physiol Sci* 60: 415–424, 2010
41. Endo Y, Suzuki M, Yamada H, Horita S, Kunimi M, Yamazaki O, Shirai A, Nakamura M, Iso-O N, Li Y, Hara M, Tsukamoto K, Moriyama N, Kudo A, Kawakami H, Yamauchi T, Kubota N, Kadowaki T, Kume H, Enomoto Y, Homma Y, Seki G, Fujita T. Thiazolidinediones enhance sodium-coupled bicarbonate absorption from renal proximal tubules via PPARγ-dependent nongenomic signaling. *Cell Metab* 13: 550–561, 2011
42. Sun D, Seki G, Uwatoko S, Nakao A, Goto A, Fujita T, Kimura S, Taniguchi S. Quantifying porphobilinogen deaminase mRNA in microdissected nephron segments by a modified RT-PCR. *Kidney Int* 61: 336–341, 2002
43. Zhou W, Hildebrandt F: Molecular cloning and expression of phospholipase C epsilon 1 in zebrafish. *Gene Expr Patterns* 9: 282–288, 2009

See related editorial, "Working Out Nephronophthisis Genetics One Family at a Time," on pages 865–868.

This article contains supplemental material online at http://jasn.asnjournals.org/lookup/suppl/doi:10.1681/ASN.2012101034/-/DCSupplemental.

Development/Plasticity/Repair

A Sensitive Period for GABAergic Interneurons in the Dentate Gyrus in Modulating Sensorimotor Gating

Nannan Guo,[1] Kaichi Yoshizaki,[1] Ryuichi Kimura,[1] Fumikazu Suto,[1,2] Yuchio Yanagawa,[3] and Noriko Osumi[1]

[1]Tohoku University Graduate School of Medicine, Sendai, Miyagi 980-8575, Japan, [2]National Institute of Neuroscience, National Center for Neurology and Psychiatry, Kodaira 187-8502, Japan, [3]Gunma University Graduate School of Medicine and Japan Science and Technology Agency CREST, Maebashi, 371-8511, Japan

Developmental perturbations during adolescence have been hypothesized to be a risk factor for the onset of several neuropsychiatric diseases. However the physiological alterations that result from such insults are incompletely understood. We investigated whether a defined perturbation during adolescence affected hippocampus-dependent sensorimotor gating functions, a proposed endophenotype in several psychiatric diseases, most notably schizophrenia. The developmental perturbation was induced during adolescence in mice using an antimitotic agent, methylazoxymethanol acetate (MAM), during postnatal weeks (PW) 4–6. MAM-treated mice showed a decrease in hippocampal neurogenesis immediately after treatment, which was restored by PW10 in adulthood. However, the mice treated with MAM during adolescent stages exhibited a persistent sensorimotor gating deficiency and a reduction in prepulse inhibition-related activation of hippocampal and prefrontal neurons in adulthood. Cellular analyses found a reduction of GABAergic inhibitory neurons and abnormal dendritic morphology of immature neurons in the dentate gyrus (DG). Interestingly, bilateral infusion of muscimol, a $GABA_A$ receptor agonist, into the DG region reversed the prepulse inhibition abnormality in MAM-treated mice. Furthermore, the behavioral deficits together with the decrease in the number of GABAergic neurons in this MAM model were rescued by exposure to an enriched environment during a defined critical adolescent period. These observations suggest a possible role for GABAergic interneurons in the DG during adolescence. This role may be related to the establishment of neural circuitry required for sensorimotor gating. It is plausible that changes in neurogenesis during this window may affect the survival of GABAergic interneurons, although this link needs to be causally addressed.

Introduction

In general, neuropsychiatric diseases, such as schizophrenia, are thought to result from a developmental defect with poorly defined etiology and pathophysiology (Weinberger, 1996; Lewis and Levitt, 2002; Rapoport et al., 2005). People who experience developmental insults in adolescence are hypothesized to be at risk for schizophrenia (Douaud et al., 2009; Gogtay et al., 2011). Therefore, studying this population could be key to understanding how abnormal neurodevelopment leads to subsequent psychopathology.

Received Jan. 3, 2012; revised Feb. 27, 2013; accepted March 2, 2013.

Author contributions: N.G., K.Y., F.S., and N.O. designed research; N.G., K.Y., R.K., and F.S. performed research; Y.Y. contributed unpublished reagents/analytic tools; N.G., K.Y., F.S., and N.O. analyzed data; N.G., F.S., and N.O. wrote the paper.

This work was supported by the Core Research for Evolutional Science and Technology from Japan Science and Technology Agency. N.G. is a postdoctoral fellow supported by Tohoku Neuroscience Global Center of Excellence. We thank Drs. Shun Nakamura, Takeo Yoshikawa, and Naoshige Uchida for their suggestions on the manuscript. We thank Ms. Ayumi Ogasawara, Sayaka Makino, and Emiko Ootsuki for the maintenance and care of the mice and for their great help with additional experiments. We are also grateful for the encouragement of all of the members of our laboratory.

The authors declare no competing financial interests.

Correspondence should be addressed to Noriko Osumi, PhD, D.D.S., Division of Developmental Neuroscience, Tohoku University Graduate School of Medicine, Sendai 980-8575, Japan. E-mail: osumi@med.tohoku.ac.jp.

N. Guo's present address: Center for Regenerative Medicine, Massachusetts General Hospital, Harvard Medical School, Boston, MA 02114.

DOI:10.1523/JNEUROSCI.0032-12.2013

 0270-6474/13/336691-14$15.00/0

During adolescence, the brain undergoes extensive synaptic remodeling, including reductions in dendritic arborization, axon myelination, and pruning of synapses (Sisk and Zehr, 2005). The integrity of these processes may be crucial for a wide range of sensory and cognitive functions that are impaired in neuropsychiatric diseases (Lewis, 1997). Thus, given the importance of the hippocampus in several psychiatric diseases (Heckers and Konradi, 2010; Tamminga et al., 2010), we wanted to know whether perturbation in a defined adolescent period could affect hippocampal functions in adulthood.

Another noticeable feature of adolescence is the developmental change of the GABA inhibitory system (Kapur and Macdonald, 1999; Fleming et al., 2007). Abnormalities in the hippocampal GABA system, including a significant reduction in the number of interneurons, reduced GABA-receptor (GABAR) expression, and the disinhibition of pyramidal cells, have been implicated in a variety of neuropsychiatric disorders, including deficient sensorimotor processes (Lewis et al., 2004; Heckers and Konradi, 2010). A recent postmortem study has demonstrated developmental changes in the expression of GABA signaling genes in the hippocampus of normal subjects and this progressive pattern of expression is disturbed in schizophrenic patients (Hyde et al., 2011).

It is difficult to fully model neuropsychiatric diseases in rodents. However, endophenotypes in rodents have received considerable attention recently owing to greater tractability for their

Table 1. Antibodies used

Antibody	Species	Working dilution	Vender
BrdU	Rat IgG2a	1:500	AbD Serotec
Caspase-3	Rabbit IgG	1:400	BD Pharmingen
c-fos	Rabbit IgG	1:500	Santa Cruz Biotechnology
Doublecortin	Rabbit IgG	1:1000	Abcam
GFP	Chicken IgY	1:500	Abcam
Parvalbumin	Mouse IgG1	1:1000	Chemicon
Anti-chicken IgG Alexa 488	Goat IgG	1:400	Invitrogen
Anti-mouse IgG Cy3	Donkey IgG	1:400	Jackson ImmunoResearch
Anti-rabbit IgG Cy3	Donkey IgG	1:400	Jackson ImmunoResearch
Anti-rat IgG Alexa 488	Goat IgG	1:400	Invitrogen

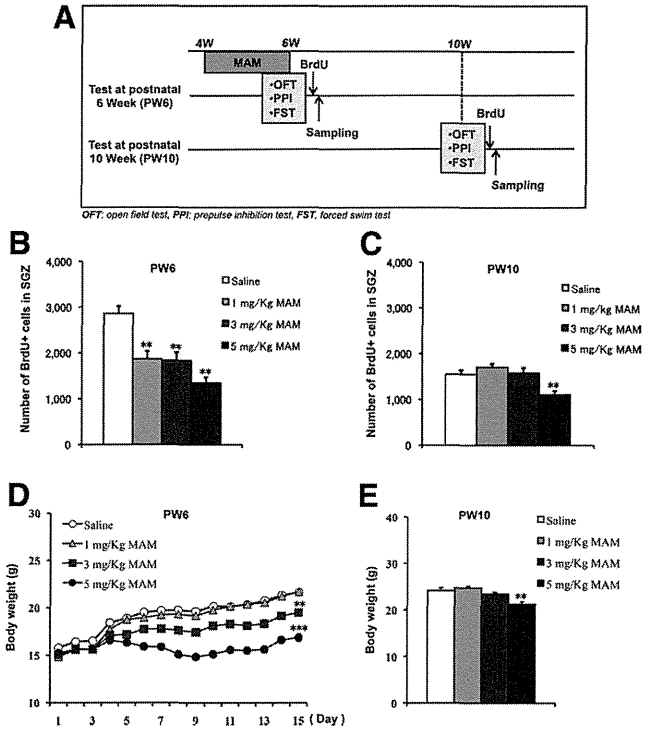

Figure 1. Decrease in newborn cell proliferation at PW6 by MAM treatment and rescue at PW10. ***A***, Experimental design for MAM treatment and behavioral tests. ***B***, ANOVA analysis revealed a significant decrease in newborn cell numbers in a dose-dependent manner immediately after 2 week MAM treatment ($F_{(3,28)} = 15.58428$, $p < 0.0001$, $n = 8$ mice for each group). ***C***, Rescue of new cell proliferation was observed 4 weeks later at PW10 ($F_{(2,21)} = 1.88832$, $p = 0.17614$ for 1 mg/kg and 3 mg/kg MAM vs saline control), except for the highest dose of MAM treatment ($F_{(1,14)} = 30.96936$, $p = 0.00007$ for 5 mg/kg MAM vs saline control, $n = 8$ mice for each group). ***D***, MAM treatment induced a dose-dependent change in body weight (repeated ANOVA: $F_{(3,44)} = 116.77$, $p < 0.001$; 1-way ANOVA at the last day of MAM treatment: $F_{(1,22)} = 0.02353$, $p = 0.87949$ for 1 mg/kg MAM vs saline control; $F_{(1,22)} = 26.76762$, $p = 0.00003$ for 3 mg/kg MAM vs saline control; $F_{(1,22)} = 106.61121$, $p < 0.0001$, $n = 12$ mice for each group). ***E***, Body weights were recovered by PW10 ($F_{(2,21)} = 2.12923$, $p = 0.14389$ at 1 mg/kg and 3 mg/kg MAM vs saline control, $n = 8$ mice for each group), except for the highest dose of MAM ($F_{(1,14)} = 13.92006$, $p = 0.00224$ for 5 mg/kg MAM vs saline control, $n = 8$ mice for each group). $^*p < 0.05$; $^{**}p < 0.01$.

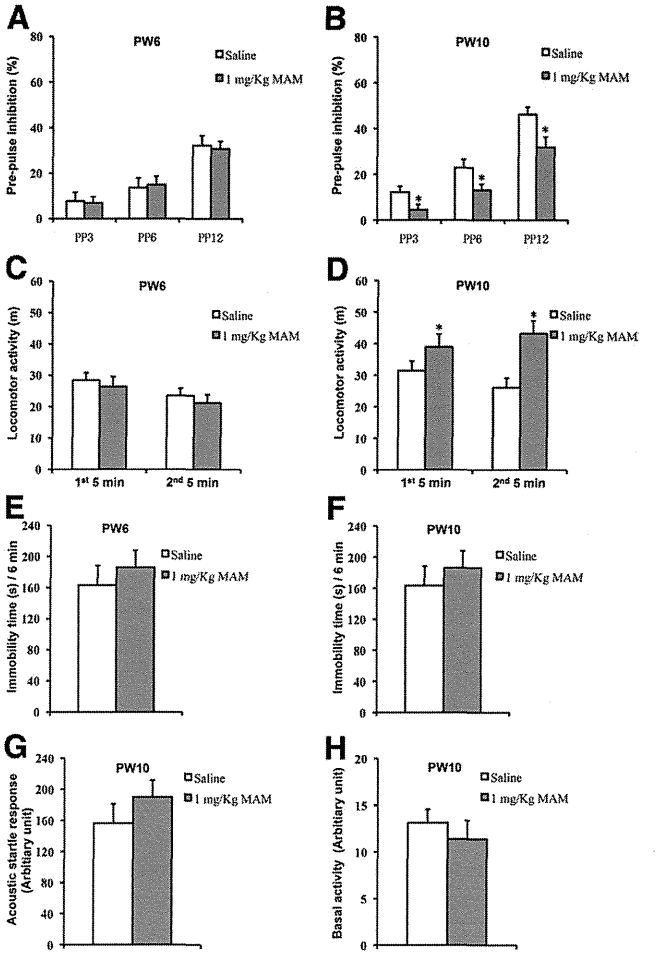

Figure 2. PPI deficiency and increased spontaneous hyperactivity were observed at PW10 but not at PW6 in MAM-treated mice. ***A***, The PPI scores were not different between the saline-treated and MAM-treated groups at PW6 (2-way ANOVA with group treatment and prepulse intensity: $F_{(2,42)} = 0.0904$, $p = 0.914$; 1-way ANOVA with PP3: $F_{(1,14)} = 0.02919$, $p = 0.86678$; PP6: $F_{(1,14)} = 0.09199$, $p = 0.76612$; PP12: $F_{(1,14)} = 0.06947$, $p = 0.9595$ for MAM vs saline, $n = 8$ for each group). ***B***, PPI deficits were observed at each prepulse intensity level in MAM-treated mice at PW10 (2-way ANOVA with group treatment and prepulse intensity: $F_{(2,42)} = 0.561$, $p = 0.575$; 1-way ANOVA with PP3: $F_{(1,14)} = 4.76369$, $p = 0.04659$; PP6: $F_{(1,14)} = 4.61941$, $p = 0.04958$; PP12: $F_{(1,14)} = 6.58918$, $p = 0.02237$ for MAM vs saline, $n = 8$ for each group). ***C***, There was no change in spontaneous activity between groups at PW6 (first 5 min, $F_{(1,10)} = 0.24641$, $p = 0.63034$; second 5 min, $F_{(1,10)} = 0.3524$, $p = 0.56594$ for MAM vs saline, $n = 6$ for each group). ***D***, Spontaneous hyperactivity was observed in the MAM group at PW10 (first 5 min: $F_{(1,12)} = 7.45188$, $p = 0.01827$; second 5 min: $F_{(1,12)} = 7.6342$, $p = 0.01718$ for MAM vs saline, $n = 7$ for each group). ***E***, ***F***, During the 6 min forced swimming test, there were no differences in the immobility times (***E***) between groups at PW6 ($F_{(1,12)} = 1.28709$, $p = 0.29987$ for MAM vs saline control, $n = 7$ for each group) or (***F***) between groups at PW10 ($F_{(1,16)} = 0.68658$, $p = 0.41952$ for MAM vs saline, $n = 9$ mice for each group). ***G***, There was no difference between the two groups in the acoustic startle response to the startle stimulus at PW10 ($F_{(1,14)} = 0.52523$, $p = 0.48056$ for MAM vs saline, $n = 8$ mice for each group). ***H***, There was no difference between the two groups in the response to the background stimulus at PW10 ($F_{(1,14)} = 0.50669$, $p = 0.48827$ for MAM vs saline, $n = 8$ mice for each group). $^*p < 0.05$ vs saline control.

objective assessment in both rodents and humans. Sensorimotor gating is one such endophenotype that can be modeled in rodents (Cadenhead et al., 2000; Louchart-de la Chapelle et al., 2005). This process can be evaluated across several species, including human beings, using prepulse inhibition (PPI) testing (Ciaroni et al., 2002; Swerdlow et al., 2008). PPI is considered an endophenotype of several neuropsychiatric diseases, including schizophrenia (Braff et al., 2001; Braff and Light, 2005). Therefore, in this study, we focused on adolescent perturbations that caused transient decreases in neurogenesis and that may relate to the formation of the hippocampal GABAergic system and proper establishment of PPI (Swerdlow and Geyer, 1998; Bast and Feldon, 2003).

Methylazoxymethanol acetate (MAM) is an alkylating agent that exerts its effects on neuroblasts undergoing their final mitosis without affecting either glial cells or quiescent cells (Haddad et al., 1972; Cattaneo et al., 1995). Moreover, MAM treatment in-

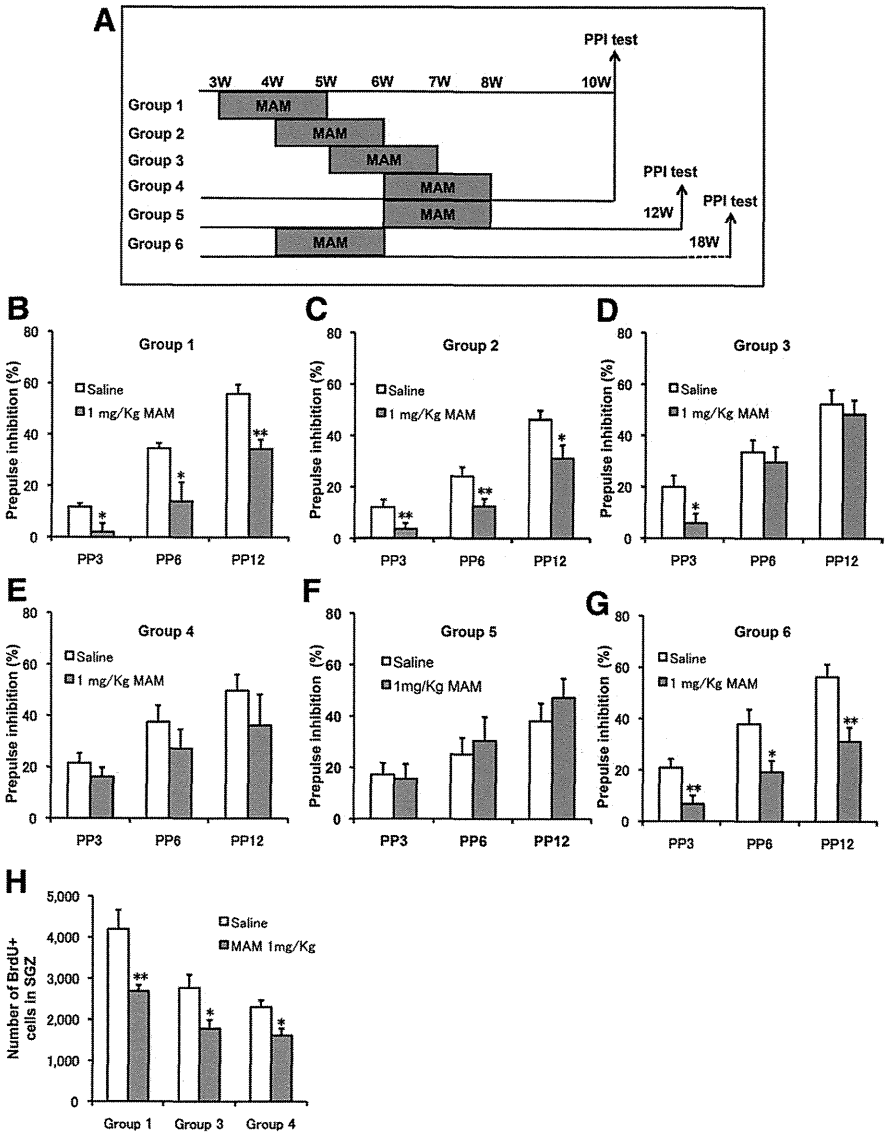

Figure 3. Developmental changes in PPI performance induced by MAM treatment. ***A***, Experimental design for MAM treatment at different periods and PPI testing at PW10 or PW18. ***B***, PPI defects were observed at PW10 in animals that received MAM treatment during PW3–PW5 (2-way ANOVA with group treatment and prepulse intensity: $F_{(2,33)} = 1.102$, $p = 0.344$; 1-way ANOVA with PP3: $F_{(1,11)} = 5.95075$, $p = 0.03286$; PP6: $F_{(1,11)} = 6.35471$, $p = 0.02844$; PP12: $F_{(1,11)} = 14.28306$, $p = 0.00305$ for MAM vs saline, $n = 7$ for saline and $n = 6$ for MAM). ***C***, PPI deficits were observed at PW10 following MAM treatment during PW4–PW6 (2-way ANOVA with group treatment and prepulse intensity: $F_{(4,36)} = 0.676$, $p = 0.613$; 1-way ANOVA with PP3: $F_{(1,13)} = 5.69986$, $p = 0.03285$; PP6: $F_{(1,13)} = 6.39256$, $p = 0.0252$; PP12: $F_{(1,13)} = 6.46156$, $p = 0.02456$ for MAM vs saline, $n = 8$ for saline and $n = 7$ for MAM). ***D***, PPI defects were observed only in PP3 at PW10 in animals that received MAM treatment during PW5–PW7 (2-way ANOVA with group treatment and prepulse intensity: $F_{(2,33)} = 0.56$, $p = 0.577$; 1-way ANOVA with PP3: $F_{(1,11)} = 4.98357$, $p = 0.04733$; PP6: $F_{(1,11)} = 0.21936$, $p = 0.64867$; PP12: $F_{(1,11)} = 0.21027$, $p = 0.65549$ for MAM vs saline, $n = 7$ for saline and $n = 6$ for MAM). ***E***, There were no changes in PPI scores due to MAM treatment during PW6–PW8 (2-way ANOVA with group treatment and prepulse intensity: $F_{(2,36)} = 0.146$, $p = 0.864$; 1-way ANOVA with PP3: $F_{(1,12)} = 0.91403$, $p = 0.35791$; PP6: $F_{(1,12)} = 0.94648$, $p = 0.34982$; PP12: $F_{(1,12)} = 0.8762$, $p = 0.3677$ for MAM vs saline, $n = 7$ for each group). ***F***, There were no changes in PPIs tested at PW12 following a 2 week MAM treatment during PW6–PW8 (2-way ANOVA with group treatment and prepulse intensity: $F_{(2,42)} = 0.319$, $p = 0.729$; 1-way ANOVA with PP3: $F_{(1,14)} = 0.05173$, $p = 0.82336$; PP6: $F_{(1,14)} = 0.22695$, $p = 0.64115$; PP12: $F_{(1,14)} = 0.81549$, $p = 0.38178$ for MAM vs saline, $n = 5$ for each group). ***G***, PPI deficits were observed at PW18 following MAM treatment during PW4–PW6 (2-way ANOVA with group treatment and prepulse intensity: $F_{(2,42)} = 0.832$, $p = 0.442$; 1-way ANOVA with PP3: $F_{(1,14)} = 10.28012$, $p = 0.00634$; PP6: $F_{(1,14)} = 7.6342$, $p = 0.01525$; PP12: $F_{(1,14)} = 13.58056$, $p = 0.00245$ for MAM vs saline, $n = 8$ for saline and $n = 7$ for MAM). ***H***, ANOVA analysis revealed that MAM treatment during PW3–PW5 (Group 1), PW5–PW7 (Group 3), or PW6–PW8 (Group 4) significantly decreased the number of newborn cells, identified by BrdU staining (Group 1: $F_{(1,14)} = 9.66715$, $p = 0.00769$; Group 3: $F_{(1,14)} = 6.89389$, $p = 0.01996$; Group 4: $F_{(1,14)} = 8.6382$, $p = 0.01078$ for MAM vs saline control, $n = 8$ mice for each group). $^{*}p < 0.05$ vs saline control; $^{**}p < 0.01$ vs saline control.

duces a transient decrease in postnatal neurogenesis, which can be rescued (Ciaroni et al., 1999). Here, we established a MAM-induced mouse model that showed a transient decrease in neurogenesis during a defined postnatal period and subsequent behavioral deficiencies in early adulthood. We propose a MAM-sensitive "vulnerable" period in adolescence, during which the dentate gyrus (DG) GABA system establishes the PPI circuitry and is modulated by enriched environment.

Materials and Methods

Animals. Three-week-old male C57BL/6J mice were purchased from Japan Charles River and were maintained in the animal facility at Tohoku University School of Medicine, Sendai, Japan. To identify GABAergic interneurons, we used heterozygous *GAD67-GFP* knock-in mice expressing GFP under the control of the endogenous *GAD67* gene promoter (Tamamaki et al., 2003). The mice were housed in pairs in standard housing conditions [cage, 25 × 18 cm (height, 15 cm); 22 ± 2°C] with a 12 h light-dark cycle (lights on at 8:00 A.M.) and with food and water available *ad libitum*. After 1 week of breeding and habituation in the animal facility, the mice were subjected to the experiments described below. All the animal experiments were performed in accordance with the National Institutes of Health guidelines for the care and use of laboratory animals and were approved by the Committee for Animal Experiments at Tohoku University.

MAM treatment and subsequent analyses. Mice were subcutaneously injected with MAM (1, 3, or 5 mg/kg) or saline once a day for 2 weeks. For 5-bromo-2-deoxyuridine (BrdU) analysis, MAM-treated mice were injected with BrdU 24 h after the last MAM injection, and were killed 2 h later. For the behavioral analyses, the MAM-treated mice rested for 0 or 4 weeks, and were then subjected to further analyses.

PPI measurements. PPI was measured as previously reported (Hayashi et al., 2008). The mice were tested in a startle chamber (SR-LAB System, San Diego Instruments). After the mice were placed into the chamber, they were allowed to habituate for a period of 10 min, during which 65 dB of white noise was generated in the background. The PPI test began and ended with five presentations of the startle trials (pulse, 120 dB; length, 40 ms), and these startle trials were excluded from the data analysis. After five startle trials, the animals randomly received 10 startle trials, 10 no-stimulus trials (pulse, 65 dB), and 30 PPI trials. The PPI trials were presented with a 68, 72, or 77 dB prepulse (i.e., 3, 6, or 12 dB higher than background, for 20 ms in length, indicated as PP3, PP6, and PP12, respectively), followed 100 ms later by a 40 ms, 120 dB pulse. Each of the three PPI trials (PP3, PP6, and PP12) was presented 10 times. The intertrial interval was between 10

and 20 s and the total session lasted ~17 min. In the study, PPI-related c-fos expression, after 10 min habituation, 30 startle trials, or PPI trials (PP3, PP6 and PP12, randomly presented 10 times each) were delivered to the mice. The percentage PPI of the startle response was calculated using the following formula: $100 - [(SRPP/SR) \times 100]$, where *SR* denotes the startle response to the pulse stimulus and *SRPP* denotes the startle response to the pulse with the prepulse stimulus.

Open-field test. The animal was placed in the center of the activity-field arena of a transparent cage [50 × 50 cm (height, 30 cm)] for 10 min. The locomotor activity of each mouse was monitored for a total of 10 min with a video camera, a tracking system, and tracking software (ANY-maze, Stoelting), which allowed total movement activity to be read out directly and calculated.

Forced swim test. A mouse was placed in a 10-cm-diameter cylinder filled with 25 ± 1°C water to a height of 10 cm and was exposed to swim stress for 7 min. The total duration of immobility during the last 6 min of the test was measured using the same tracking system used in the open-field test.

Exposure to enriched environment. Four or five mice were raised together in a large cage [40 × 30 cm (height, 20 cm)] with running wheel, toys, extra nesting material, and small plastic houses and tubes. The objects were rearranged every 2 weeks. The enriched environment (EE) was maintained for 6 weeks [during postnatal weeks (PW) 4–10] or 4 weeks (during PW6–PW10). All of the groups were counterbalanced for saline or MAM treatment; therefore multiple groups of animals were generated: standard housing with saline injection, standard housing with MAM injection, 6 week or 4 week enriched housing with saline injection, and 6 week or 4 week enriched housing with MAM injection.

Elevated plus maze. This apparatus consisted of a plus-shaped maze elevated 60 cm from the floor and comprised two opposing open arms (25 × 5 cm each) and two arms of the same dimensions enclosed by 30-cm-high walls with an open roof. In addition, a 1-cm-high clear Plexiglas edge surrounded the open arms to prevent falls. Each animal was placed in the middle of the maze facing the open arm. Following 10 min of testing, the animals were returned to their home cages. Arm preference was automatically analyzed using ANY-maze video tracking software.

Immunohistochemistry. Immunohistochemistry was performed as described previously (Matsumata et al., 2012). Briefly, mice were anesthetized with sodium pentobarbital (40 mg/kg, i.p.) and were transcardially perfused with 0.9% NaCl solution (preheated at 37°C), followed by fixation with 4% paraformaldehyde dissolved in 0.01 M phosphate-buffer saline (PBS) at 4°C. After decapitation, the brains were removed from the skull and submerged in a series of sucrose solutions from (10, 20, and 30%) until they sank. The frozen brains were sectioned into 16-μm-thick coronal sections using a cryostat (CM3050, Leica). The sections were washed with Tris-buffered saline containing Tween 20, pH 7.4. For immunostaining, the cryostat sections were incubated with primary antibodies overnight at 4°C and were then incubated at 4°C for 2 h with the appropriate secondary antibodies. Fluorescently labeled sections were visualized using either a confocal laser scanning microscope (LSM5 PASCAL, Carl Zeiss, http://www.Zeiss.com) or a fluorescence microscope (AxioPlan2, Carl Zeiss; BZ-9000, Keyence) using a 20× objective lens. Images of single optical sections were captured and recorded digitally. Information concerning the antibodies used in this study is presented in Table 1.

BrdU labeling, immunofluoresence, and quantification of labeled cells. Mice were intraperitoneally injected with BrdU at 25 or 50 mg/kg body weight (10 mg/ml stock, dissolved in 0.9% saline), and brains were collected either 2 h or 4 weeks after BrdU injection to visualize the prolifer-

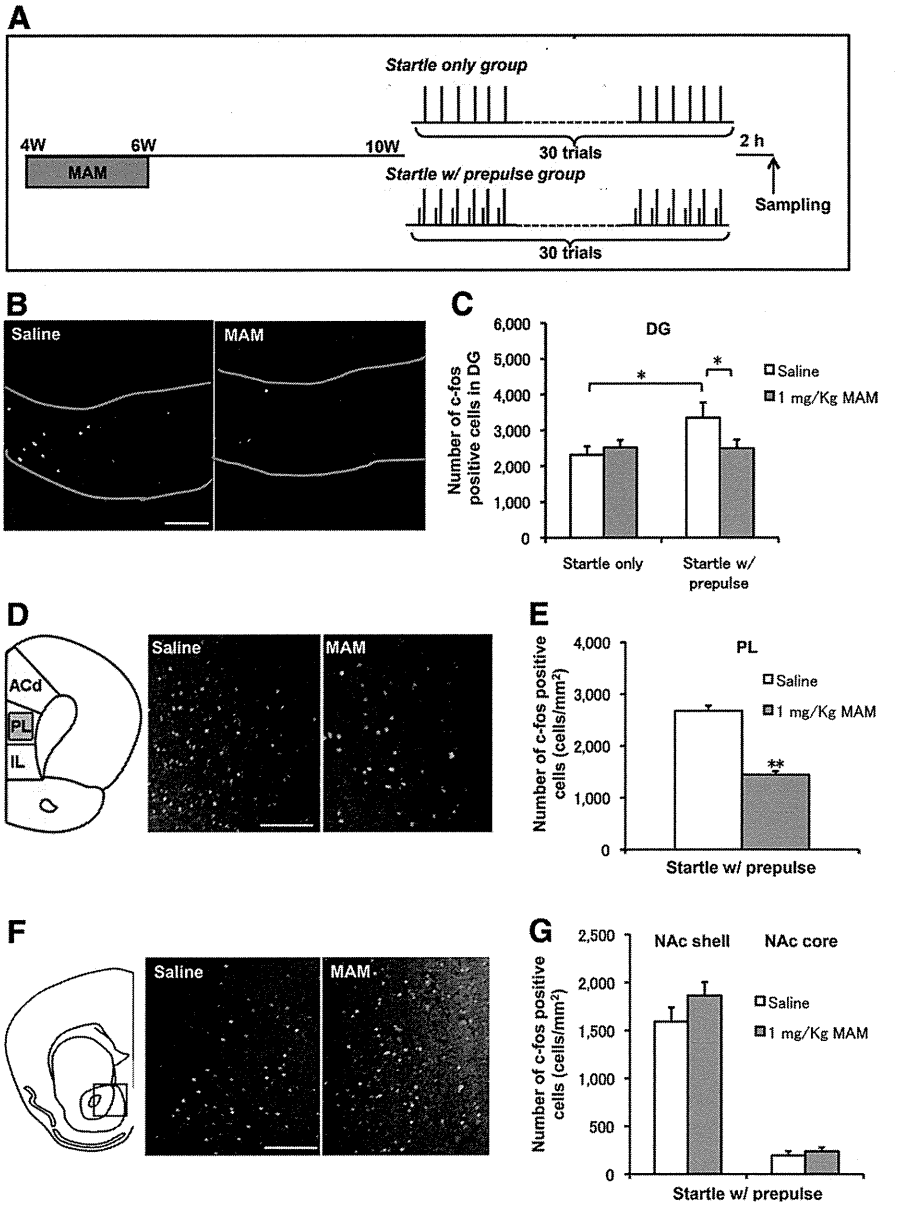

Figure 4. PPI-induced hippocampal activation was blocked by MAM treatment. ***A***, Experimental design of MAM treatment and the behavioral manipulation protocol. ***B***, Representative c-fos staining in the DG. ***C***, There was an increase in the number of c-fos+ cells in the startle-with-prepulse group compared with the startle-only group ($F_{(1,14)} = 4.62166$, $p = 0.04953$ startle with prepulse plus saline vs startle only plus saline, $n = 8$ for each group), but this increase was blocked by MAM treatment during PW4–PW6 ($F_{(1,16)} = 4.54244$, $p = 0.4892$ for startle with prepulse plus MAM vs startle with prepulse plus saline, $n = 8$ for startle with prepulse plus saline and $n = 10$ for startle with prepulse plus MAM). ***D***, Representative c-fos staining in the PL cortex. ***E***, MAM treatment decreased the number of c-fos+ cells in the PL cortex ($F_{(1,18)} = 89.19019$, $p < 0.001$ for startle with prepulse plus MAM vs startle with prepulse plus saline, $n = 10$ for each group). ***E***, Representative c-fos staining in the nucleus accumbence (NAc). ***F***, There were no changes in c-fos+ cells in the NAc shell and NAc core between groups (NAc shell: $F_{(1,20)} = 1.79051$, $p = 0.19588$ for MAM vs saline control, $n = 11$ for each group; NAc core: $F_{(1,14)} = 0.56137$, $p = 0.4611$ for MAM vs saline $n = 8$ mice for each group). Scale bar, 200 μm. $^*p < 0.05$; $^{**}p < 0.01$.

ation and survival of hippocampal newborn cells. Before incubation with an anti-BrdU antibody, the frozen sections (16 μm) were boiled in 0.01 M citric acid for 15 min, incubated in 2N HCl for 10 min at 37°C, and washed in 0.01 M PBS. For quantification analyses, BrdU+ cells, caspase3+ cells, c-fos+ cells, and parvalbumin+ cells were counted throughout rostra-caudal extension of the DG. The c-fos+ cells in the prelimbic (PL) cortex and nucleus accumbens were restricted to two discrete points from 2.34 and 1.70 mm bregma. Because the brightness of c-fos+ cells varied with different intensity, we set a brightness threshold at 200% of the background level; cell nuclei darker than the threshold value were not considered to be positive for c-Fos and were not counted. Quantification of doublecortin+ (DCX+) cell density was restricted to two discrete points from bregma that represented the anterior (−1.94 mm from bregma) and posterior (−2.92 mm from bregma) DG. DCX+ cells were morphologically categorized into two groups according to previously established criteria (Plümpe et al., 2006, see results). Approximately 300 DCX+ cells were analyzed per animal. Every sixth section of the hippocampus was used for cell counting, and the total number of positive cells was obtained by multiplying the value by 6.

Muscimol administration. For cannula implantation, mice were anesthetized with sodium pentobarbital (60 mg/kg, i.p.) and fixed in a stereotaxic frame (Narishige SN-2). A pair of cannulae were implanted bilaterally with stainless steel guide cannulae (8 mm; 26 gauge) aimed at the DG region (bregma, −2.0 mm; lateral, ±1.5 mm; depth, 1.5 mm). Dummy cannulae were inserted into the guide cannulae to reduce the risk of infection. The mice recovered for at least 7 d before receiving behavioral training. The $GABA_AR$ agonist muscimol (Sigma-Aldrich) was diluted in saline, and 10 or 100 ng was administered to each side of the brain. Fluorescein isothiocyanate (FITC) (Jackson ImmunoResearch), either 50 or 500 ng per hemisphere, was bilaterally injected into the region of DG to visualize the spread of the muscimol. The mouse was gently held during drug infusion. The dummy cannula was removed from the guide cannula. An injection needle (30 gauge; length, 8.8 mm) was inserted into the guide cannula to a depth of 0.8 mm lower than the guide cannula (depth, 1.5 mm). Muscimol was bilaterally infused into the DG region (1.0 μl to each hemisphere) at a rate of 0.2 μl/min. The infusion was administered 15–20 min before the PPI test. The injection needle remained in the guide cannula for an additional 3 min after the infusion was completed. Then, the dummy cannula was reinserted into the guide cannula.

Statistics. Data in the text and figures are expressed as the means ± SEM, and were analyzed using ANOVA, or ANOVA repeated measures. The body weights of the saline-treated and MAM-treated mice were analyzed using a one-way ANOVA for the body weight at the final injection day and the repeated ANOVA for body weight over injection time. The PPI experiments were analyzed using two-way ANOVAs with group treatment and prepulse intensity as the between-subject factors. This is followed by a one-way ANOVA for the single prepulse intensities tested. All statistical analysis was conducted using STATISTICA (StatSoft). $p < 0.05$ was defined as statistically significant.

Results

MAM treatment during the adolescent stage induced sensorimotor gating deficits in young adults

To optimize the appropriate conditions of MAM treatment for later experiments, we first determined the dose of MAM required for a robust depletion of newborn cells without impairment of the overall health of the mice (Fig. 1). As established in the literature, adolescence occurs during postnatal days 28–42 in male rodents (Spear, 2000). Therefore, we first target PW4–PW6 in mice. Treatment with 1 mg/kg MAM per day during PW4–PW6 (Fig. 1*A*) effectively blocked neurogenesis and preserved body weight at PW6 levels, and neurogenesis returned to the control levels at PW10. Higher concentrations caused a slightly greater blockade of neurogenesis but body weight was also significantly affected (Fig. 1*B–E*). We examined the sensorimotor gating function using the PPI paradigm at both PW6 and PW10. At PW10,

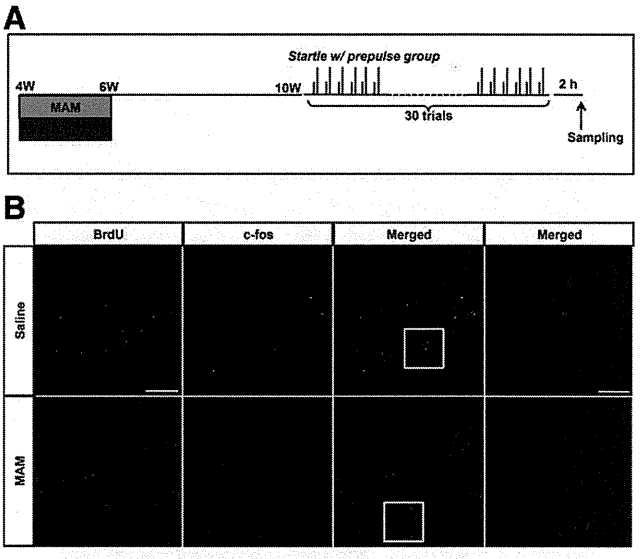

Figure 5. Representative double staining for c-fos and BrdU within the DG at PW10. ***A***, Experimental design of MAM treatment, BrdU injection, and the behavioral manipulation protocol. ***B***, Representative double staining for c-fos and BrdU within the DG at PW10. Scale bars: single labeled images, 200 μm; merged images, 50 μm.

but not at PW6, a significant reduction in PPI was observed for all prepulse levels (Fig. 2*A*,*B*). The acoustic startle response and the response to background were unchanged at PW10 (Fig. 2*G*,*H*).

To gain greater insight into the general physical state of MAM-treated mice, we performed the behavioral tests at PW6 and PW10. As shown, spontaneous locomotor activity was unchanged between the two groups at PW6, but MAM-treated mice became hyperactive at PW10 (Fig. 2*C*,*D*). MAM treatment did not induce depression-like behavior, as measured by either the immobility time within the recording period (Fig. 2*E*,*F*) or by the latency to first immobility (one-way ANOVA, $F_{(1,16)} = 0.57682$, $p = 0.45861$ for MAM vs saline) in the forced swim test during the juvenile stage or in early adulthood.

Therefore, MAM treatment during the adolescent stage transiently decreased hippocampal neurogenesis and specifically impaired sensorimotor gating and locomotor activity in early adulthood.

Developmental effects of MAM treatment on PPI scores

We next examined the PPI scores of mice treated with MAM during four different postnatal periods (Fig. 3*A*). As shown in Figure 3*B*, MAM treatment during PW3–PW5 produced a deficit in PPI at PW10 at all the prepulse levels. Similar results were obtained for MAM treatment during PW4–PW6 (Fig. 3*C*). PPI impairment was also observed at PW18 (Fig. 3*G*), suggesting a persistent effect of MAM treatment on PPI deficiency. However, when mice were exposed to MAM during PW5–PW7, the reducing effect of MAM treatment on PPI was observed only for the PP3 prepulse level at PW10 (Fig. 3*D*). The mice treated with MAM during PW6–PW8 exhibited no significant difference at any prepulse intensity level at either PW10 (Fig. 3*E*) or PW12 (Fig. 3*F*). Regarding neurogenesis, all of the groups displayed a similar reduction in the number of BrdU+ cells immediately after MAM treatment (Figs. 1*B*, 3*H*), showing that the MAM treatment was effective in all conditions. As mentioned above, when MAM treatment began after PW6, the PPI deficit was not observed. These results indicate a defined postnatal period dur-

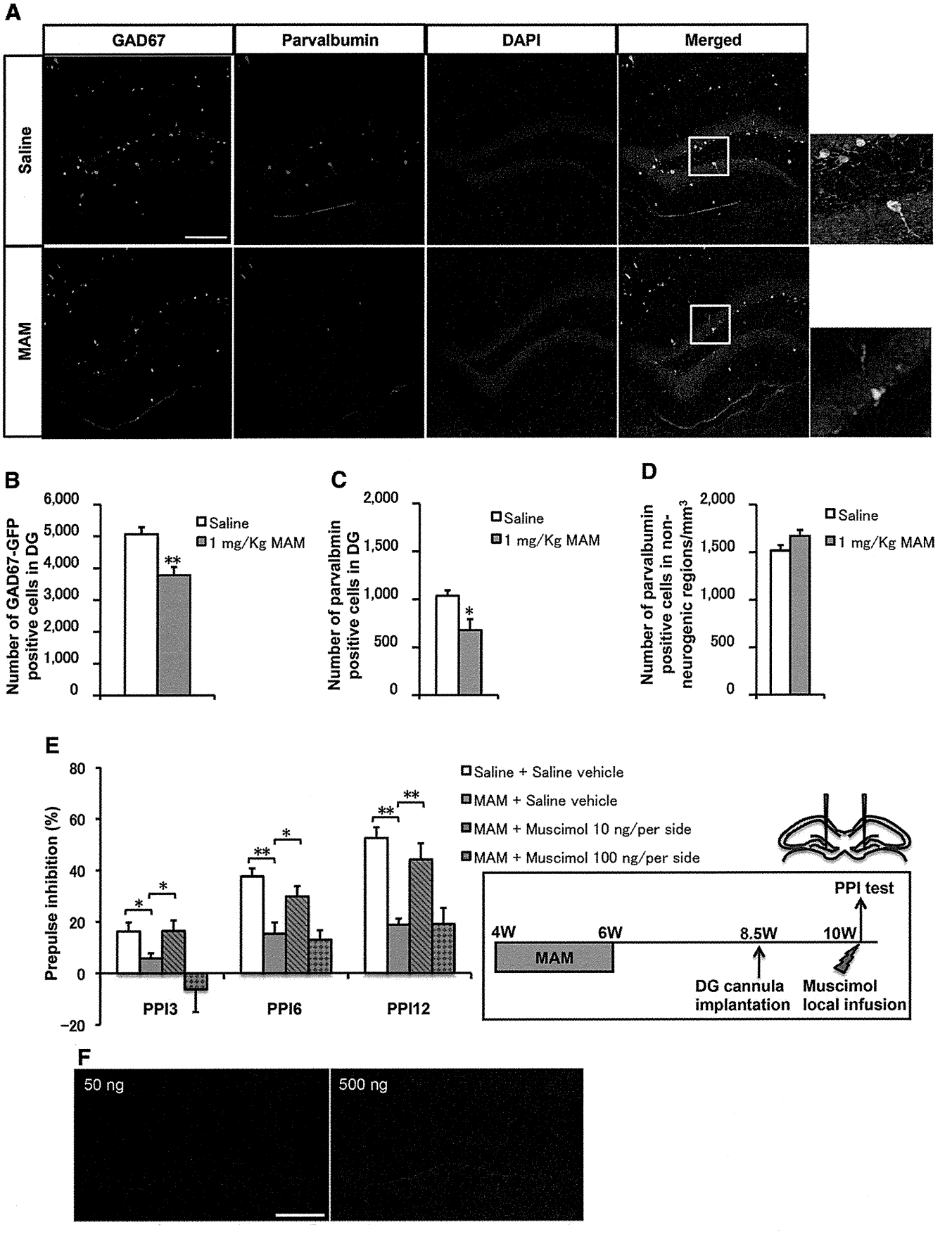

Figure 6. MAM-treated mice showed decreased numbers of GABA interneurons and PPI deficits rescued by a 6 week EE application and local DG infusion of the $GABA_AR$ agonist muscimol. ***A***, Representative GAD67-EGFP and PV staining in the DG. Scale bar, 200 μm. ***B***, ***C***, The numbers of (***B***) GAD67-EGFP+ cells ($F_{(1,14)} = 14.90636$, $p = 0.00173$ for MAM vs saline, $n = 8$ for each group) and (***C***) PV+ cells ($F_{(1,14)} = 7.85009$, $p = 0.01413$ for MAM vs saline, $n = 8$ for each group) in the DG were decreased by MAM treatment. ***D***, There were no changes in (*Figure legend continues.*)

ing which MAM perturbation leads to PPI deficits that persist into adulthood.

PPI-associated hippocampal activation was blocked by MAM treatment

To further identify how hippocampal dysfunction affects sensorimotor gating function in our mouse model, we examined neuronal activation in the DG after PPI testing. Mice were treated with saline or MAM from PW4 to PW6, as described previously. Concurrently, a low dose of BrdU (25 mg/kg) was delivered during this period to evaluate newborn cells. Four weeks later, each group of mice was exposed to 30 trials of a startle stimulus, either with or without a prepulse. The mice were scarified 2 h later (Fig. 4*A*). ANOVA analysis revealed a significant increase in the number of c-fos+ cells in the startle-with-prepulse group compared with the startle-only group with saline treatment ($p = 0.049$), but this increase was completely ameliorated by MAM treatment compared with the startle-only group with MAM treatment ($p = 0.93$) (Fig. 4*B*). Furthermore, startle-with-prepulse testing with MAM treatment induced a significant decrease in the number of c-fos+ cells, but this effect was not observed in the startle-only group (Fig. 4*B*,*C*). However, only a few of the BrdU+ cells that survived for 4–6 weeks were positive for c-fos (4 of 467; Fig. 5). These data consistently indicate that MAM perturbation during the "critical period" causes decreased hippocampal neurogenesis and impaired DG activation in the PPI paradigm, which suggests the noncell autonomous involvement of the newborn cells in the establishment of the PPI circuit.

We examined PPI-associated activation in other brain regions to further determine the effects of MAM treatment. In PL cortex (Fig. 4*D*), which receives an efferent projection from the ventral hippocampus (Saint Marie et al., 2010), the number of c-fos+ cells in MAM-treated mice was significantly decreased compared with the saline group (Fig. 4*E*). However, in the shell or the core of the nucleus accumbence, there was no change in PPI-associated c-fos expression between the saline and MAM groups (Fig. 4*F*,*G*). These results exclude a global toxic effect of MAM treatment but instead emphasize a specific dysfunction of the hippocampus and PL cortex in the PPI-related regulatory neural circuitry in our animal model.

Disturbance of the GABA system by MAM treatment

As mentioned earlier, MAM treatment caused impaired hippocampal neurogenesis in adolescence and reduced activation of the DG during PPI testing. However, the c-fos+ neurons detected shortly after PPI task were not granule cells newly generated during the critical period because c-fos+ cells in the DG were rarely positive for BrdU (Fig. 5). These data suggest that MAM treatment during adolescence modulates neuronal activation through other mechanisms that may not be linked to changes in neurogenesis. Therefore, we examined changes in inhibition, as inhibition in the DG is critical for maintaining a sparse pattern of activation and optimal function of the DG in encoding. We used GAD67-GFP knock-in mice (Tamamaki et al., 2003; Hoskison et al., 2007; Doischer et al., 2008) to quantify the number of GABAergic interneurons. We also examined parvalbumin (PV)-containing GABAergic neurons that provide inhibitory input to the perisomatic region of principal cells.

Mice were exposed to MAM during PW4–PW6, and the total number of GFP+ and PV+ neurons in the DG were analyzed at PW10 (Fig. 6*A*). In the DG, exposure to MAM resulted in a significant decrease in the total number of GFP+ and PV+ interneurons (Fig. 6*B*,*C*). In contrast, the total number of PV+ cells was not altered in the non-neurogenic cornu ammonis areas (i.e., CA1, CA2, and CA3 regions) (Fig. 6*D*). Therefore, the influence of MAM treatment on inhibitory circuit was specific to the DG although MAM may directly affect the inhibitory system, suggesting a developmental consequence of neurogenic ablation during the critical adolescent stage.

To further examine the GABA system deficiency in our animal model, we investigated the effect of $GABA_AR$ activation against MAM treatment (Fig. 6*E*). Mice were exposed to MAM from PW4 to PW6 and, 4 weeks later, the $GABA_AR$ agonist muscimol (10 or 100 ng per hemisphere) was bilaterally infused into the DG region 15–20 min before PPI testing (Fig. 6*E*, left). Saline was infused as a vehicle control. MAM treatment from PW4 to PW6 produced a significant deficit at every prepulse intensity level (Fig. 6*E*). The MAM-induced PPI deficits were rescued by a bilateral acute infusion of 10 ng per hemisphere muscimol into the DG (Fig. 6*E*). However, the higher dose of muscimol, 100 ng per hemisphere, failed to rescue the PPI deficits. The similar molar amount of florescent dye of FITC was injected into DG to visualize the spread of the muscimol. As shown, FITC was restricted to the DG without spreading into the CA1 or CA3 region of hippocampus (Fig. 6*F*). These results indicate that the GABAergic abnormality in the DG is associated with the deficient PPI phenotype in our animal model, and further suggest that the balance between excitatory and inhibitory inputs might be significant for the proper establishment of PPI.

Rescue of PPI deficits by exposure to EE

To further examine the link between the decrease in neurogenesis and the impairment in PPI performance, we applied an EE regimen, which increased neurogenesis in the DG (Kempermann et al., 1997). Mice were treated with MAM from PW4 to PW6 and were maintained in an EE from PW4 to PW10 (6 week EE application) or normal conditions. At PW10, the PPI scores and other behavioral abnormalities of the mice were evaluated (Fig. 7*A*). Although an EE application did not alter PPI performance in mice without MAM treatment (Fig. 7*B*), a 6 week exposure to an EE restored the PPI deficits that had been induced by MAM treatment at all the prepulse intensity levels (Fig. 7*B*). In addition, MAM-induced spontaneous hyperactivity in the open-field test (Fig. 7*C*) was also rescued by the 6 week EE application. Furthermore, we examined the effects of the EE application on anxiety behavior in the elevated plus maze test. MAM-treated mice spent significantly less time in open arms than the control mice, and this difference was rescued by a 6 week EE application (Fig. 7*D*).

←

(*Figure legend continued.*) the numbers of PV+ cells in non-neurogenic regions (CA1, CA2, and CA3) ($F_{(1,14)} = 2.7165$, $p = 0.12157$ for MAM vs saline, $n = 8$ samples for each group). ***E***, The groups of mice were bilaterally implanted with cannulae into DG at PW8.5 and locally infused with muscimol at PW10 (left). As shown, PPI deficits were observed in the MAM group at PW10 (2-way ANOVA with group treatment and prepulse intensity: $F_{(9,44)} = 0.885$, $p = 0.546$; 1-way ANOVA with PP3: $F_{(1,10)} = 6.80619$, $p = 0.03119$; PP6: $F_{(1,10)} = 17.16855$, $p = 0.00324$; PP12: $F_{(1,10)} = 49.75486$, $p = 0.000113$ for saline plus saline vehicle group vs MAM plus saline vehicle group) and these deficits were further rescued by a local DG muscimol infusion of 10 ng/per hemisphere (PP3: $F_{(1,10)} = 5.36461$, $p = 0.04921$; PP6: $F_{(1,10)} = 6.0888$, $p = 0.03886$; PP12: $F_{(1,10)} = 14.19858$, $p = 0.00548$ for MAM plus saline vehicle group vs MAM plus 10 ng/per hemisphere muscimol group), but not by a local DG muscimol infusion of 100 ng/per hemisphere (PP3: $F_{(1,10)} = 1.77437$, $p = 0.21954$; PP6: $F_{(1,10)} = 0.16899$, $p = 0.6918$; PP12: $F_{(1,10)} = 0.00142$, $p = 0.97089$ for MAM plus saline vehicle group vs MAM plus 100 ng/per hemisphere muscimol group, $n = 6$ mice for each group). ***F***, Representative images for bilaterally local injection of FITC (left, 50 ng/per hemisphere; right, 500 ng/per hemisphere) into DG to visualize the spread of muscimol. Scale bar, 200 μm. $^*p < 0.05$; $^{**}p < 0.01$.

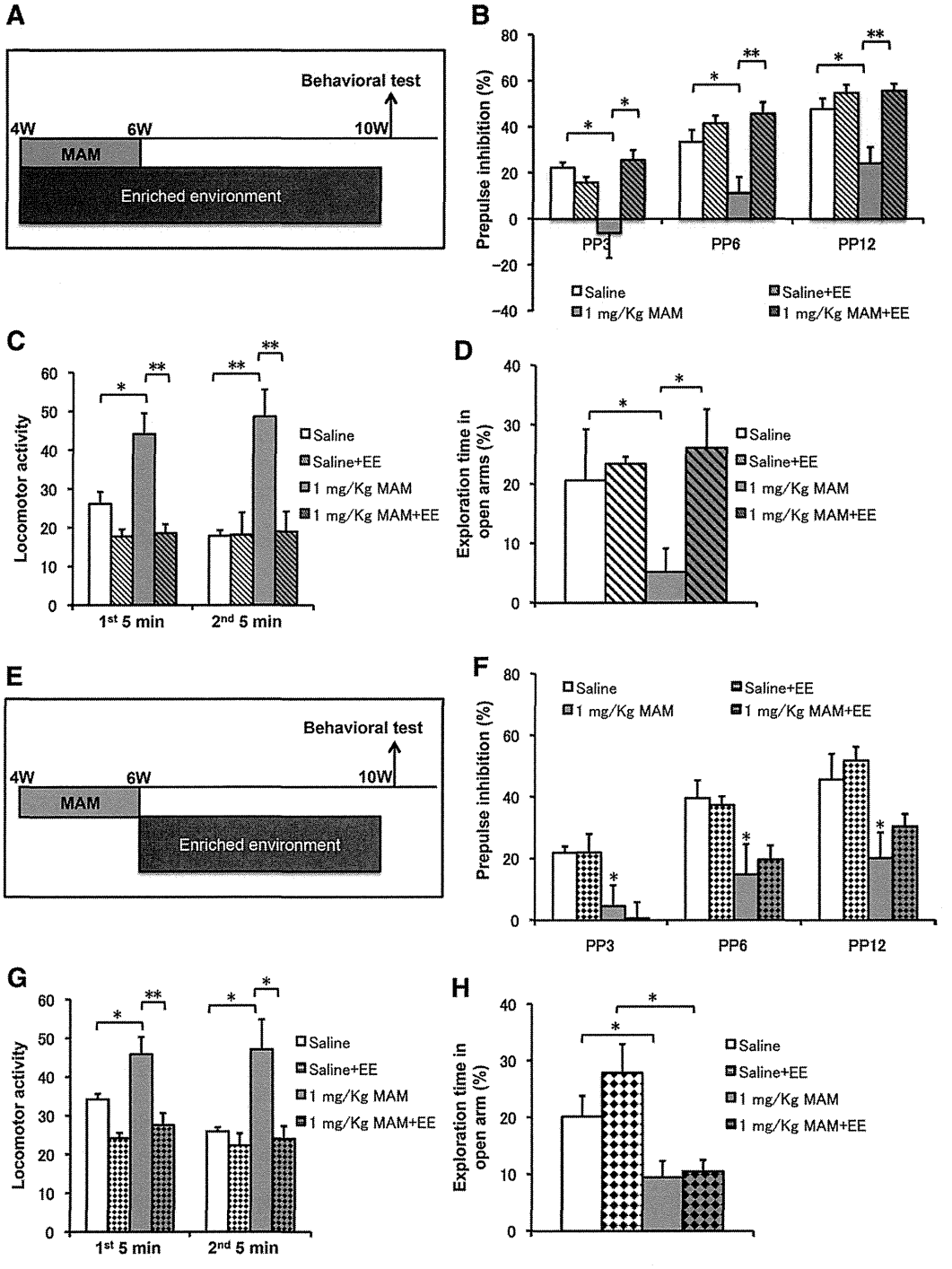

Figure 7. Behavioral defects in MAM mice were rescued by an EE application that included PW4–PW6. ***A***, Experimental design for MAM treatment, EE application during PW4–PW10, and PPI testing. ***B***, MAM group displayed PPI deficits, which were rescued by an EE application during PW4–PW10 (2-way ANOVA with group treatment and prepulse intensity: $F_{(9,44)} = 0.999, p = 0.455$; 1-way ANOVA with blue bar, PP3: $F_{(1,10)} = 5.35715, p = 0.04934$; PP6: $F_{(1,10)} = 5.52419, p = 0.04666$; PP12: $F_{(1,10)} = 6.53438, p = 0.03384$ for MAM vs saline; hatched blue bar, PP3: $F_{(1,10)} = 6.01467, p = 0.03978$; PP6: $F_{(1,10)} = 13.71342, p = 0.00602$; PP12: $F_{(1,10)} = 13.79835, p = 0.00592$ for MAM plus EE vs MAM, $n = 6$ for each group). ***C***, The spontaneous hyperactivity in the MAM group was rescued by EE application during PW4–PW10 (first minutes: $F_{(1,10)} = 8.44982, p = 0.01565$ for MAM vs saline; $F_{(1,10)} = 19.25921, p = 0.00136$ for MAM plus EE vs MAM; second 5 min: $F_{(1,10)} = 26.81883, p = 0.00023$ for MAM vs saline; $F_{(1,10)} = 23.71114, p = 0.00039$ for MAM plus EE vs MAM, $n = 6$ for each group). ***D***, Anxiety-like behaviors in the MAM group were also rescued by EE application ($F_{(1,10)} = 6.33847, p = 0.03051$ for MAM vs saline, $F_{(1,10)} = 10.00856, p = 0.0101$ for MAM plus EE vs MAM, $n = 6$ for each group). $^*p < 0.05$; $^{**}p < 0.01$. ***E***, Experimental design for MAM treatment, EE application during PW6–PW10 and PPI testing. ***F***, The MAM group displayed PPI deficits that were not rescued by an EE application during PW6–PW10 (2-way ANOVA with group treatment and prepulse intensity: $F_{(9,56)} = 0.902, p = 0.53$; 1-way ANOVA with blue bar, PP3: $F_{(1,10)} = 5.03714, p = 0.04864$; PP6: $F_{(1,10)} = 10.97326, p = 0.00784$; PP12: $F_{(1,10)} = 7.63621, p = 0.02001$ for MAM vs saline; hatched blue bar, PP3: $F_{(1,10)} = 0.90189, p = 0.36466$; PP6: $F_{(1,10)} = 0.45422, p = 0.51561$; PP12: $F_{(1,10)} = 0.00407, p = 0.9504$ for MAM vs saline, $n = 6$ for each group). ***G***, The spontaneous hyperactivity in the MAM group was rescued by EE application during PW6–PW10 (first minutes: $F_{(1,10)} = 6.17334, p = 0.03229$ for MAM vs saline; $F_{(1,10)} = 11.23893, p = 0.00733$ for MAM plus EE vs MAM; second 5 min: $F_{(1,10)} = 7.35725, p = 0.02184$ for MAM vs saline; $F_{(1,10)} = 7.53281, p = 0.02067$ for MAM plus EE vs MAM, $n = 6$ mice for each group). ***H***, Anxiety-like behaviors in the MAM group were also rescued by EE application ($F_{(1,10)} = 5.25848, p = 0.04477$ for MAM vs saline; $F_{(1,10)} = 0.55739, p = 0.4725$ for MAM plus EE vs MAM, $n = 6$ mice for each group). $^*p < 0.05$; $^{**}p < 0.01$.

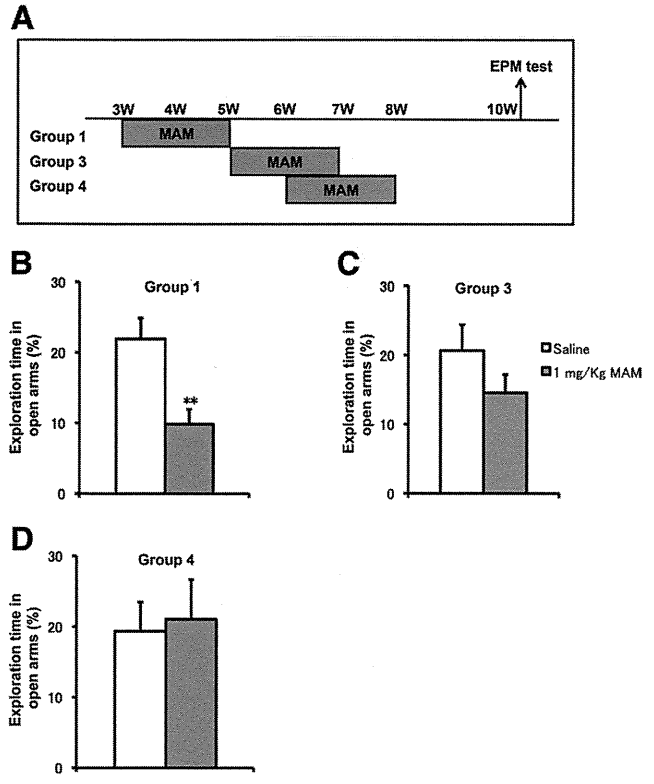

Figure 8. Developmental changes in the elevated plus maze (EPM) test induced by MAM treatment. ***A***, Experimental design for MAM treatment at different periods and EPM testing at PW10. ***B***, Anxiety-like behaviors were observed at PW10 in animals that received MAM treatment during PW3–PW5 ($F_{(1,14)} = 11.11031$, $p = 0.00493$ for MAM vs saline, $n = 8$ for each group). ***C***, ***D***, Mice with MAM treatment at PW5–PW7 (***C***) and PW6–PW8 (***D***) showed normal behavioral phenotypes compared with the saline group in the EPM test at PW10 (PW5–PW7: $F_{(1,14)} = 1.76874$, $p = 0.2048$; PW6–PW8: $F_{(1,14)} = 0.06245$, $p = 0.80629$ for MAM vs saline, $n = 8$ for each group). $^{*}p < 0.05$ vs saline control; $^{**}p < 0.01$ vs saline control.

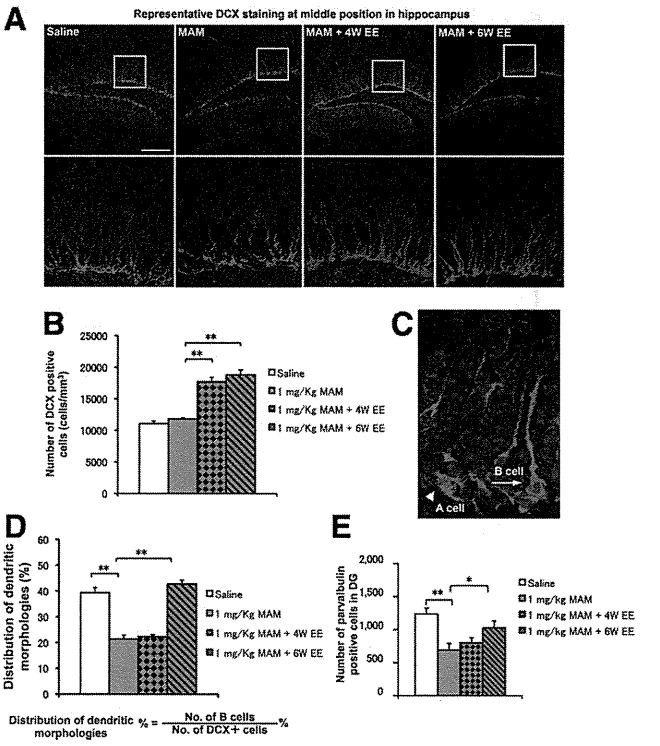

Figure 9. Morphological deficits in DCX+ cells were rescued by EE application in MAM-treated mice. ***A***, Representative DCX staining in the DG in each group. Scale bar, 200 μm. ***B***, The total number of DCX+ cells in the saline (open bar) and MAM (blue bar) groups was comparable in the DG ($F_{(1,14)} = 3.0005$, $p = 0.1052$ for MAM vs saline). EE application significantly increased the number of DCX+ cells ($F_{(2,21)} = 58.27158$, $p < 0.001$, $n = 8$ for each group). ***C***, Representative DCX morphology without (category A cell) and with (category B cell) strong vertical processes. ***D***, The proportion of category B cells was significantly decreased in the MAM group ($F_{(1,14)} = 80.53699$, $p < 0.001$ for MAM vs saline) but was rescued by a 6 week EE application ($F_{(1,14)} = 173.91939$, $p < 0.001$ for MAM plus 6 week EE vs MAM) but not by a 4 week EE application ($F_{(1,14)} = 1.89102$, $p = 0.19069$ for MAM plus 4 week EE vs MAM, $n = 8$ for each group). ***E***, The decrease in the number of PV+ cells was rescued by a 6 week EE application ($F_{(1,14)} = 16.87865$, $p = 0.00106$ for MAM vs saline; $F_{(1,14)} = 5.56777$, $p = 0.03335$ for MAM vs MAM plus 6 week EE, $n = 8$ samples for each group) but not by a 4 week EE application ($F_{(1,14)} = 0.72633$, $p = 0.40842$ for MAM vs MAM plus 4 week EE, $n = 8$ for each group). $^{*}p < 0.05$; $^{**}p < 0.01$.

Therefore, all three abnormal behavioral phenotypes (PPI deficits, hyperactivity, and anxiety), which were induced by MAM treatment during PW4–PW6, could be reversed by placing the mice in an EE during the 2 week MAM treatment.

To further examine the critical period during which the rescue effects were delivered by EE application, we designed another experiment to perform a 4 week EE application from PW6 to PW10, which excluded the 2 week MAM-treatment period (Fig. 7*E*). In contrast to the 6 week EE application, the 4 week EE application that excluded the critical period failed to rescue the MAM-induced PPI deficits (Fig. 7*F*). Regarding the other tests, the 4 week EE application decreased MAM-induced spontaneous hyperactivity (Fig. 7*G*), which is consistent with a previous report (Brenes et al., 2008). However, the same 4 week EE did not rescue the MAM-induced anxiety behavior (Fig. 7*H*). An ANOVA analysis comparing the 6 and 4 week EE against the MAM group ($p = 0.045$) confirmed a rescue by the 6 week EE but not by the 4 week EE treatment. That is, the difference in anxiety levels in the mice exposed to EE results from the exclusion of the 2 week period of MAM treatment during the EE exposure.

To further address the critical period, we also examined the anxiety-related behaviors of mice treated with MAM at three different stages (Fig. 8*A*). As shown, mice treated with MAM during PW3–PW5 spent less time in the open arms of the maze than the control group (Fig. 8*B*), whereas those treated either during PW5–PW7 (Fig. 8*C*) or during PW6–PW8 (Fig. 8*D*) did not show any significant differences when compared with the control group. We also confirmed that, for mice treated with MAM during PW4–PW6, EE application during PW6–PW12 ameliorated hyperactivity but failed to rescue PPI deficits or anxiety-related behaviors (data not shown). Together, these results demonstrate the existence of a defined period for postnatal environmental intervention, which is subsequently related to the establishment of PPI and anxiety-related behaviors but not to hyperactivity. This observation proposes a beneficial role of an EE during the adolescent critical period against the onset of schizophrenia-like behaviors in early adulthood.

Morphological deficit in DCX+ cells was recovered by 6 week EE

We next examined how the different manipulations affected cellular phenotypes in the brain in the newborn neurons (Fig. 1*C*). We focused on a population of DCX+ cells, transient amplifying cells, and postmitotic immature neurons (Plümpe et al., 2006).

We estimated the density of DCX+ cells in the saline group, the MAM-treated group, the MAM-plus-4-week-EE group (EE application excluding the 2 week MAM treatment), and the MAM-plus-6-week-EE group (EE application including the 2 week MAM treatment) (Fig. 9*A*). There was no change in the